

1 **Making Aircraft Vortices Visible to Radar by Spraying Water into the Wake**

2 Karim Shariff*

3 *NASA Ames, Moffett Field, California, 94035*

4 **Corresponding author address: NASA Ames, Moffett Field, California, 94035*

5 E-mail: Karim.Shariff@nasa.gov

ABSTRACT

6 Aircraft trailing vortices pose a danger to following aircraft during take-off
7 and landing. This necessitates spacing rules, based on aircraft type, to be
8 enforced during approach in IFR (Instrument Flight Regulations) conditions;
9 this can limit airport capacity. To help choose aircraft spacing based on the
10 actual location and strength of the wake, it is proposed that wake vortices can
11 be detected using conventional ground-based precipitation and cloud radars.
12 This is enabled by spraying a small quantity water into the wake from near the
13 wing. The vortex strength is revealed by the doppler velocity of the droplets.
14 In the present work, droplet size distributions produced by nozzles used for
15 aerial spraying are considered. Droplet trajectory and evaporation in the flow-
16 field is numerically calculated for a heavy aircraft, followed by an evaluation
17 of radar reflectivity at 6 nautical miles behind the aircraft. Small droplets
18 evaporate away while larger droplets fall out of the wake. In the humid condi-
19 tions that typically prevail during IFR, a sufficient number of droplets remain
20 in the wake and give good signal-to-noise ratios (SNR). For conditions of av-
21 erage humidity, higher frequency radars combined with spectral processing
22 gives good SNR.

1. Introduction

a. Motivation

Aircraft trailing vortices are a hazard to following airplanes during take-off and landing (e.g., Barbagallo 2014). For a review of their dynamics, see Spalart (1998). Due to their mutually induced velocity, a pair of trailing vortices generally descends from the altitude where it was generated. (For exceptions to this in strongly stratified conditions, see Spalart, 1996). Therefore, a wake encounter may occur when a following aircraft finds itself below¹ the path of the leading aircraft. The possibility for this is increased during take-off and landing, and the present work addresses the latter situation. When cleared for a visual approach to landing, the pilot of the following aircraft can visually attempt to remain above the path of the leader by, for example, flying at a higher glide slope to the same touchdown point as the leader. Even in visual approaches, however, things can and do go awry (Barbagallo 2014, §2.3). This means that efforts to find an all-weather wake sensor should be continued.

When the ceiling is less than 1000 ft and the visibility less than 3 statute miles, operations must be conducted under Instrument Flight Regulations (IFR). In this case, air traffic controllers maintain separations according to the weight categories of the leading and following aircraft; see Table 1. These separations have started to limit capacity at some airports (Crouch et al. 2001b) and we refer the reader to a report (Broderick et al. 2008) by a committee of the National Research Council entitled “Wake Turbulence: An Obstacle to Increased Air Traffic Capacity.” About two decades ago, NASA initiated the AVOSS (Aircraft Vortex Spacing System) program whose aim was to make aircraft spacing dynamic through a combination of vortex sensing and real-time flowfield simulation. The present work is motivated by the vortex detection aspect of the AVOSS

¹A former colleague, Dr. Vernon Rossow, has long suggested that with GPS and fly-by-wire, the simplest approach to wake avoidance would be for a following aircraft to remain at or above the path of the leader.

45 program. A current effort that has similar aims as the defunct AVOSS program is WakeNet-
46 Europe (www.wakenet.eu). Finally, we mention the development of a system to hasten the break-
47 up of trailing vortices by exciting vortex instabilities through periodic motion of control surfaces
48 (Crouch et al. 2001a,b). Such a system could be implemented together with one for wake detection.

49 *b. Previous work using radar to detect aircraft wakes*

50 The main vortex detection technology tested by the AVOSS program was infrared ground-based
51 lidar. A concern raised about lidar was that since water vapor strongly absorbs infrared, it would
52 not be usable in IFR conditions. Another concern is that optical systems are more expensive and
53 difficult to maintain than radar. These concerns motivate consideration of radar. The next two sub-
54 sections discuss the two contexts in which previous work on the radar reflectivity of aircraft wakes
55 has been performed, namely, clear air reflectivity and the exploitation of natural precipitation; see
56 Barbaresco et al. (2016) for a recent review.

57 1) CLEAR AIR REFLECTIVITY

58 The first observational and theoretical efforts on ground-based radar detection of wakes were
59 in the context of *clear air*. Systematic tests by Gilson (1992) showed that the wake of a C-5A
60 aircraft could be detected by radars having 2–7 MW of peak power at frequencies from 0.162
61 to 5.67 GHz, with no return at 35 GHz. Shariff and Wray (2002) analyzed the reflectivity in
62 Gilson’s test using a model of a vortex pair descending in a stratified atmosphere, carrying with
63 it an oval of atmospheric air from the altitude at which the wake formed. This leads to a gradient
64 in refractive index between the oval and ambient air. Another mechanism investigated by Shariff
65 and Wray (2002), which has peak reflectivity at a low frequency of 50 MHz, is the pressure
66 (hence density) gradient in each vortex. Both of these mechanisms have some drawbacks for

67 practical use: (a) the radar cross-section is small (-60 to -80 dB m²); (b) the first mechanism
68 depends on atmospheric stratification, which has seasonal, geographic, and diurnal variations;
69 and (c) the frequency of the second mechanism is the same as that of Stratospheric-Tropospheric
70 radars, which have an antenna array on the ground looking upward. For the present application,
71 technology would have to be developed for aiming the radar by use of phasing. Li et al. (2011)
72 (see also Vanhoenhacker-Janvier 2012) extended the work of Shariff and Wray (2002) with a better
73 calculation of the compressibility-induced variation in air density in the wake. More importantly,
74 they showed that the atmospheric gradient of water vapor is wound up into a spiral by each vortex,
75 which allows scattering at high frequencies. Unfortunately, radar reflectivity is not studied beyond
76 an evolution time of 40 s which corresponds to 1.7 nm behind the aircraft.

77 Barbaresco et al. (2008) conducted tests using an X-band (9.6 GHz) radar for aircraft taking-off
78 and flying straight and level at 1500 m altitude. For the take-off case, the range was about 700 m
79 looking roughly sideways using peak pulse power of only 20 W. For the aircraft at an altitude of
80 1500 m, the radar was looking straight up and the peak pulse power was 75 W. A time doppler plot
81 indicated a spiral structure in each vortex. However, in staring mode, a return is obtained for only
82 five seconds, at most. Barbaresco et al. (2008) did not report how far downstream of the aircraft
83 the wake could be detected; it appears that this distance is very short.

84 In conclusion, clear air reflectivity is an interesting prospect, but more careful and better docu-
85 mented observational campaigns combined with theoretical efforts are needed.

86 2) EXPLOITING NATURAL PRECIPITATION

87 A different approach, which the author first heard about from Robert Neece (NASA Langley,
88 personal communication) around 2000, exploits the fact that water droplets (in the form of fog
89 or rain) are present in IFR weather conditions. They are strong radar reflectors, and, when an

90 airplane wake sets these particles into motion, they can be separated from ambient droplets via
91 their doppler signature. This strategy has the advantage that standard doppler weather radars could
92 be used. Seliga and Mead (2009) demonstrated the feasibility of the approach using a W-band (94
93 GHz) radar in light rain in an opportunistic test with only 100 mW of peak power. An analysis
94 of the reflectivity of this mechanism has been conducted by Liu et al. (2013) and Li et al. (2016)
95 for rain and fog, respectively. In Spring 2011, successful measurements (Barbaresco et al. 2012)
96 in rain were obtained at Paris (Charles De Gaulle) Airport in using a Thales BOR-A 550 X-band
97 radar with only 20 W peak power; see Barbaresco (2012) for more legible figures. The results of
98 a campaign (also in rain) during Fall 2012 are reported in Barbaresco et al. (2014), which presents
99 plots at different times in three-dimensions. The main drawback of this approach is that there
100 may be long periods of time, and stretches along the wake in which a sufficient number of natural
101 droplets is unavailable.

102 *c. Present approach and concept of operations*

103 The approach proposed here is related to the use of natural precipitation for wake detection
104 discussed in the previous paragraph, except that, to provide a persistent radar target, water spray
105 is injected into the wake. We envision one nozzle on each side of the airplane that injects the
106 water spray near the wing trailing edge at a specified spanwise location. One possibility for nozzle
107 placement is the aft tip of a flap track fairing. A pump and water tank could be located nearby
108 within the wing.

109 The present work considers a single ground-based radar, placed between the two outermost
110 approach paths of several parallel runways in order that it can monitor all approach paths. The
111 choice of radar coordinates is described in detail in §2m. Most of the results presented are for the
112 radar looking (with normal incidence) at the wake cross-section 6 nm behind the aircraft. The radar

113 can also perform an azimuthal scan to monitor several wake cross-sections along the flight paths;
114 see §3i. However the off-normal cross-sections have a reduced SNR due to increased range and a
115 reduction in doppler velocity by the cosine of the angle relative to the normal. Given successful
116 detection of a wake, pilots could be presented with that information on a heads-up display and be
117 cleared for an approach using that information.

118 The main constraint imposed by nature is droplet retention in the wake: a spray nozzle produces
119 a distribution of droplet sizes; the smallest droplets evaporate away while the largest ones fall
120 out of the wake due to gravity. However, IFR conditions are correlated with high humidity (§21).
121 This reduces the rate of evaporation and makes the approach feasible. In a non-IFR case we
122 consider that has moderate humidity, only the Ka and W band radars give sufficient reflectivity in
123 a patch above each vortex. However, it is shown that spectral processing reduces noise and allows
124 detection even when the signal to noise ratio in individual pulse returns is < 1 . Finally, there is
125 no reason why the present approach and that of using natural precipitation could not be combined
126 using the same radar. It should be noted that spray droplets can also be detected using lidar: they
127 would enhance the signal-to-noise ratio compared to natural aerosols and therefore reduce the
128 required power.

129 **2. Calculation methods**

130 *a. General procedure*

131 We use aircraft centered coordinates (x, y, z) , where x is streamwise, y is spanwise, and z is
132 vertical. Air and water are denoted by subscripts ‘a’ and ‘w’, respectively.

133 The calculation has three steps. The first creates a sample of droplet radii $a(t)$ from a size dis-
134 tribution pertinent to aerial spray nozzles. The second step generates a spray trail on the starboard

side of the aircraft wake. This involves injecting droplets from the sample into the wake, tracking the position $\mathbf{X}(t)$ of each droplet and its radius $a(t)$ as it evaporates. The flow-field model consists of two counter-rotating vortices whose height decreases with downstream distance x behind the aircraft. The third and final step mirrors the starboard trail to the port side and, for a given set of radar parameters, computes the reflectivity of both trails together.

Since it is prohibitive to track all of the actual droplets, the spray trail computed in step two consists of a certain number, N_{comp} , of computational droplets. In the reflectivity calculation, each computational droplet is taken to represent a multiplicity, M_{true} , of actual droplets, which is simply the ratio of the desired injected volume to the volume injected in the computation. A test showing that this procedure has achieved statistical convergence is presented in §3e.

The equations for droplet motion and evaporation are integrated using the routine LSODE which is described in Radhakrishnan and Hindmarsh (1993) and available from NETLIB. The routine chooses a time step based on a specified error tolerance. Since the flow-field model we have adopted is steady in a reference frame moving with the aircraft, it is not necessary to inject droplets at every time step, which would continuously increase the number of computational droplets. Instead, droplets are injected only during a certain time interval Δt_0 at the beginning of the calculation. This set of droplets is then evolved for successive Δt_0 intervals and appended to a file at the end of every Δt_0 interval. At the end of the computation, the file contains a spray trail that is 7 nm miles long, whose radar reflectivity we subsequently analyze. In actual practice, an aircraft would likely not generate a trail of several nautical miles behind it. Rather, it would release the spray for a short period at pre-selected locations during its approach.

A detailed description of each part of the calculation procedure is described in the following subsections. The evaporation calculation is described in §B of the online Supplemental Materials . To avoid stiffness of the system of evolution equations, droplets are removed from the calculation

when their radius becomes $< 20 \mu\text{m}$; at this point their reflectivity is too small to significantly affect the received power.

b. Droplet trajectory

The position $\mathbf{X}(t)$ and velocity $\mathbf{U}(t)$ of a droplet of mass m_d evolves according to

$$\frac{d\mathbf{X}}{dt} = \mathbf{U}(t), \quad (1)$$

$$\frac{d\mathbf{U}}{dt} = \mathbf{F}_D/m_d - g_{\text{eff}}\hat{\mathbf{z}}, \quad (2)$$

where $g_{\text{eff}} = (1 - \rho_a/\rho_w)g$ is the effective gravity accounting for buoyancy. The drag force \mathbf{F}_D is given by

$$\mathbf{F}_D = C_D \frac{1}{2} \rho_a |\mathbf{u}_{\text{rel}}|^2 \pi a^2 \frac{\mathbf{u}_{\text{rel}}}{|\mathbf{u}_{\text{rel}}|}, \quad (3)$$

where

$$\mathbf{u}_{\text{rel}} = \mathbf{u}(\mathbf{X}) - \mathbf{U}, \quad (4)$$

is the velocity of the air flow, $\mathbf{u}(\mathbf{X})$, relative to the droplet. Evaluation of the drag coefficient, C_D , is described in §A of the online Supplemental Materials.

c. Droplet size distribution of aerial spray nozzles

When the water jet issues from the nozzle, it will encounter a blast of free-stream air with a speed of 77.2 m s^{-1} . A comparable situation in the literature is that of a cylindrical liquid jet surrounded by an annulus of co-flowing air (Lorenzetto and Lefebvre 1977; Varga et al. 2003) which shows that much smaller droplets are produced than for the case of still air (with the same velocity of the liquid jet). This is due to the occurrence of both the Kelvin-Helmholtz instability and Rayleigh-Taylor instabilities. The former is driven by the shear between the air and liquid flow and leads to a smaller instability wavelength. The latter arises due to the acceleration of liquid droplets by

the drag force of the air stream. If the droplets are too small, they quickly evaporate. To produce larger droplets, both instabilities can be mitigated by reducing the relative velocity between the liquid jet and free-stream air. This is accomplished by increasing the driving pressure. However, if the droplets are too large, they fall out of the wake. Hence, there is an optimum droplet size.

We were fortunate that an experimental study (Fritz and Hoffmann 2015), which uses a wind-tunnel to mimic the free stream air flow, has recently been performed to characterize the droplet size distribution produced by nozzles used for aerial agricultural spraying. This study did indeed show that larger pressures produce larger droplets. Dr. B. Fritz kindly provided us with an Excel program, developed from that study, which gives parameters of the droplet size distribution for various nozzles, free-stream speeds, and driving pressures. Use of these parameters is now described.

Let $p(a)$ be the probability density such that $p(a)da$ is the probability that the droplet radius is in the interval $[a, a + da]$. The log-normal distribution

$$p(a) = \frac{1}{\sqrt{2\pi}a\sigma} e^{-\ln^2(a/a_0)/2\sigma^2}, \quad (5)$$

with parameters a_0 and σ , is commonly used in the spray literature. Fritz's Excel program provides information about the function $Q(a)$, defined to be the fractional volume occupied by droplets of radius $\leq a$. One can show from appropriately integrating (5) that

$$Q(a) = \frac{1}{2} (1 + \operatorname{erf} \xi), \quad (6)$$

where

$$\xi \equiv \frac{1}{\sqrt{2}\sigma} [\ln(a/a_0) - 3\sigma^2]. \quad (7)$$

The Excel program provides $a_{0.5}$ and $a_{0.9}$ defined such that $Q(a_{0.5}) = 0.5$ and $Q(a_{0.9}) = 0.9$. Using them, (6) can be numerically inverted to yield the parameters a_0 and σ of the log-normal

distribution (5). The Excel program also provides $a_{0,1}$, which we did not use because we wished to nail the size distribution for large droplets which contribute most to reflectivity.

d. Choice of nozzle

What is the best drop size distribution? A set of N_d droplets over which the incident beam is assumed to have uniform intensity, has a reflectivity proportional to (e.g., Doviak and Zrnić 1984, p. 58)

$$\zeta = \sum_{i=1}^{N_d} a_i^6, \quad (8)$$

assuming Rayleigh scattering. Maximizing this subject to fixed volume of water and fixed N_d gives the result that all droplets must be of the same size. Given this result, maximizing ζ with respect to the number N_d subject to fixed volume gives $N_d = 1$, i.e., all the volume must be in one droplet. However, such a droplet would likely fall too rapidly. To minimize droplet loss by sedimentation, droplets must not have a terminal velocity larger than the vortex descent speed, $W_{\text{descent}} = 1.75$ m s⁻¹ in the present case. Consulting the terminal velocity plot in Pruppacher and Klett (1997, p. 416) we conclude that a must be ≤ 200 μm . Hence the best distribution is uniform with a drop radius $a = 200$ μm . Since the rate of droplet evaporation is $\propto 1/a$, i.e., small droplets evaporate faster than larger ones, the above conclusion is not altered by including evaporation.

The above considerations suggest that the following “rate of ζ ” could be used to initially evaluate different nozzles without having to perform an evaporation and reflectivity calculation:

$$\dot{\zeta}_{\text{nozzle}}^< \equiv \frac{1}{\Delta t} \sum_{i: a_i < 200 \mu\text{m}}^{N_d(\Delta t)} a_i^6, \quad (9)$$

where the $<$ superscript on $\dot{\zeta}$ denotes the exclusion from the sum of large droplets which fall away, and $N_d(\Delta t)$ denotes the number of droplets produced by the nozzle in a period Δt . This value of $\dot{\zeta}_{\text{nozzle}}^<$ as a simple *a priori* measure will be tested against the full reflectivity calculations in §3h.

215 Table 2 lists the parameters for four candidate nozzles and operating conditions that
 216 were selected from B. Fritz’s Excel program. The nozzles were selected based on hav-
 217 ing a peak probability density at a large radius (which rarely exceeded $100\ \mu\text{m}$) and
 218 a high flow-rate. The flow-rate for nozzle 1 was provided by Calvin Kroes (pri-
 219 vate communication) of CP Products. For nozzles 2 and 3, flow-rates were extrap-
 220 olated from the values of 5.30 gpm and 2.45 gpm, respectively, at 60 psi reported
 221 on the manufacturer’s data sheets (www.translandllc.com/wp-content/uploads/2015/08/Aerial-Flow-Chart-20152.pdf and www.cppproductsinc.com/images/stories/downloads/Misc-Tables/A1-Web%20Aerial%20Tip%20Rate%20Chart.pdf). The extrapolations assumed a square-root depen-
 222 dence of flow-rate on pressure (Lefebvre 1989, p. 157) expected from Bernoulli’s principle, and
 223 which the manufacturer’s data follows well. For nozzle 4, the flow-rate versus pressure provided
 224 on the manufacturer’s website has a linear rather than square-root dependence. We are grateful to
 225 Dr. Brad Fritz (USDA) for measuring the actual flow-rate for us. It turned out to be much lower
 226 than the value provided by on the website.

229 *e. Droplet injection in the computation*

230 Let the origin of coordinates be in the symmetry plane of the aircraft (which corresponds to
 231 $y = 0$) with the same axial and vertical location as the droplet injector. Droplets are injected in
 232 a grid pattern within a square of width w_{square} in the yz -plane. The pattern consists of $n_{\text{square}} \times$
 233 n_{square} droplets. The square is centered at $(x, y, z) = (0, fb/2, 0)$, where f represents the fractional
 234 spanwise distance from the aircraft center plane to the wing-tip, and was chosen to be $f = 0.5$. A
 235 square shape was chosen because the nozzles we have selected are not of the flat fan type. The
 236 streamwise extent of the computed mist trail was chosen to be $\ell_{\text{trail}} = 7\ \text{nm}$ (168 seconds of elapsed

time from injection) since we wish to detect the trail at 6 nm, the longest distance for which one would want to detect the wake of a heavy aircraft under current separation rules; see Table 1.

The square pattern is injected n_x times and the time interval between injections is Δt_{inject} , whose value is chosen so that the x spacing between droplets is the same as in the cross-sectional (yz) plane. After a time period $\Delta t_0 \equiv n_x \Delta t_{\text{inject}}$, an $n_{\text{square}}^2 \times n_x$ slab of particles has been injected, which is then advanced for successive Δt_0 periods to form the entire trail. Inertial particles with a small Stokes number tend to an attractor (Haller and Sapsis 2008; Sapsis and Haller 2010) independent of injection location, and therefore where droplets end-up should be insensitive to where they are injected. A brief check on insensitivity to initial conditions will be presented in §3c.

The initial velocity of droplets is set equal to the air velocity, which is justified as follows. From the equations of droplet motion, (2)–(4), the characteristic relaxation time for a droplet to start following a new air speed, imposed at $t = 0$, say, is

$$\tau_{\text{relax}} \equiv \left| \frac{1}{u_{\text{rel}}} \frac{du_{\text{rel}}}{dt} \right|_0^{-1} = \frac{16}{3} \frac{\rho_w}{\rho_a} \frac{a^2}{v_a} (\text{Re } C_D)_0^{-1}. \quad (10)$$

where the subscript ‘0’ means that the quantity is calculated at $t = 0$. From this, the characteristic relaxation distance, $\ell_{\text{relax}} = u_{\text{rel}}(0) \tau_{\text{relax}}$ can be evaluated. Note that the initial air speed relative to the water jet is given by $u_{\text{rel}}(0) = U_{\text{app}} - U_{\text{exit}}$, where U_{app} is the approach velocity of the aircraft given in Table 3, and U_{exit} is the exit velocity of the water jet given in Table 2. The experiment of Fritz and Hoffmann (2015) measured the size distribution 1.8 m downstream of the nozzle for all straight-stream nozzles. This value is from a private communication from B. Fritz and represents a correction from a value of 1.5 m reported in Fritz and Hoffmann (2015). Figure 1b plots ℓ_{relax} as a function of drop radius for nozzle 1. Inspecting it together with the size distribution in Figure 1a, we conclude that most of the droplets are following the air stream at the measurement station of the experiment. If this had not been the case and there had been a relative velocity large enough

259 to give Weber numbers $\gtrsim 10$, then it would have been necessary to model further droplet break-up
 260 using a secondary break-up model (e.g., Apte et al. 2003).

261 *f. Flowfield of two counter-rotating wing-tip vortices*

262 We consider an aircraft flying straight and level at altitude $z_0 = 0$ in aircraft coordinates. The
 263 velocity field of the airflow in the wake is denoted by lower case $\mathbf{u}(\mathbf{x})$. This velocity field consists
 264 of the free stream, $U_{\text{app}}\hat{\mathbf{x}}$ (where U_{app} is the approach speed of the aircraft), superposed with the
 265 flow induced by a pair of counter-rotating vortices with circulations $\pm\Gamma$. The centerline of each
 266 vortex is at spanwise location $y_{\text{vort}} = \pm b_0$. Due do their mutually induced velocity, the height
 267 $z_{\text{vort}}(x)$ of the vortex pair decreases with distance x behind the wing as follows:

$$z_{\text{vort}}(x) = z_0 - W_{\text{desc}}t, \quad (11)$$

268 where $W_{\text{desc}} = \Gamma/2\pi b_0$ is the descent speed of the vortex pair. The quantity $t = x/U_{\text{app}}$ is time
 269 since the vortex at x was shed from the wing.

270 Each vortex induces a circumferential velocity $u_\theta(r)$ in the cross-plane (yz). For $u_\theta(r)$, a profile
 271 fit to flight data by P. Spalart (Private communication) of Boeing is used:

$$u_\theta = \frac{\Gamma}{2\pi r} \begin{cases} 1188.59\eta^2, & \eta < 0.0103; \\ \left[1 + (1.27 + 0.25 \log \eta)^{-14}\right]^{-1/14}, & \text{otherwise;} \end{cases} \quad (12)$$

272 where $\eta \equiv r/b_0$.

273 For an elliptically loaded wing, lifting line theory (Batchelor 1967) gives the vortex spacing as

$$b_0 = \frac{\pi}{4}b, \quad (13)$$

274 where b is the wingspan, and the vortex circulation as

$$\Gamma = \frac{W}{\rho_a U_{\text{app}} b_0}, \quad (14)$$

where W is the aircraft weight. We use the parameters for a typical heavy aircraft given in Table 3.

g. Calculation of the received signal and power

A pulse-doppler radar transmits a train of square wave pulses that modulate a carrier wave of frequency $f = 2\pi/\omega$. The duration of each pulse is τ and the pulse repetition frequency is f_{PRF} . After each pulse is transmitted, the transmit-receive switch is set to the receive position and the incoming signal is sampled. Each sample at time t is said to come from the *range gate* $r = c(t - t_t)/2$, where t_t is the transmit time of the pulse and the factor of two accounts for the round-trip. Throughout, we consider the case where the transmitting and receiving antenna are the same, the so-called mono-static case.

1) RESOLUTION SHELL

An important concept is that of the *resolution volume*, $\mathcal{R}_\tau(t)$, at time t , associated with a single pulse of finite duration, τ (e.g., Yuter 2003, p. 1836). It is defined as the volume from which a signal is received *at a fixed time* t due to scattering by the pulse. Let t_t mark the beginning of the pulse at the transmitter. A signal from a scatterer at distance r will be received in the time interval

$$t - t_t = 2r/c + \xi\tau, \quad 0 \leq \xi \leq 1, \quad (15)$$

where $\xi = 0$ corresponds to leading edge of the pulse and $\xi = 1$ to its trailing edge. Solving (15) for r gives

$$r = c(t - t_t - \xi\tau)/2, \quad 0 \leq \xi \leq 1. \quad (16)$$

Equation (16) defines a spherical shell (called the resolution volume) from which a signal is received at the fixed time t . The next subsection describes how the complex voltage received at a given time is evaluated by summing the complex voltages from each droplet in the resolution volume.

2) RECEIVED POWER AND SIGNAL-TO-NOISE RATIO

The material in this subsection is adapted from the texts Doviak and Zrnić (1984) and Ishimaru (1978). Let the “voltage” of the transmitted pulse be (the real part of)

$$V_t(t) = \begin{cases} V_0 e^{i\omega t}, & t \leq \tau; \\ 0, & \text{otherwise;} \end{cases} \quad (17)$$

where V_0 is a complex amplitude, τ is the pulse width, and “voltage” is defined such that the instantaneous transmitted power is $P_t(t) = V_t(t)V_t^*(t)$. The voltage at the input terminals of the receiver is (the real part of) the following summation over droplets:

$$V(t) = \sum_{m=1}^{N_d} A_m(t) e^{i\omega_m(t-2r_m/c)}, \quad (18)$$

where A_m is a complex scattering amplitude and

$$\omega_m \equiv \omega (1 - 2u_m/c) \quad (19)$$

is the twice doppler-shifted frequency (u_m being the radial velocity of the m th droplet) and r_m is the distance to each droplet. The summation in (18) is taken over the N_d droplets in the resolution volume associated with the pulse.

The complex scattering amplitude due to each droplet is

$$A_m = \left[\frac{\lambda^2 \ell_w \ell_B}{(4\pi)^3} \frac{G^2(\theta_m)}{r_m^4} \sigma_{bm} \right]^{1/2} V_0 \exp(i\phi_m). \quad (20)$$

The first factor in (20), namely $[\cdot]^{1/2}$, is copied from the square root of the radar equation (e.g., Doviak and Zrnić 1984, p. 34) for power, where λ is the wavelength, and σ_{bm} is the back-scattering cross-section of each droplet. The function $G(\theta_m)$ is the gain function of the antenna at the droplet, which we have assumed to depend on its angle θ_m from the beam centerline. Two loss factors (< 1) have been included in (20): ℓ_w is the two-way waveguide loss and ℓ_B is the loss due to finite

bandwidth of the receiver; values assumed for the present study are given in Table 4. The last factor in (20), $\exp(i\phi_m)$, accounts for the phase shift induced by back-scattering at the m th droplet. The back-scattering cross-section and phase-shift (σ_{bm} and ϕ_m , respectively) will be discussed further in §2k.

Radar receivers have electronics that can obtain the real and imaginary parts (denoted I and Q) of $V(t)$ and compute the instantaneous received power

$$P_r(t) = I(t)^2 + Q(t)^2 = V(t)V^*(t). \quad (21)$$

We note in passing that $I(t)$ and $Q(t)$ are the components of the real part of $V(t)$ that are in-phase and 90° out-of-phase with the transmitted carrier, respectively. Substituting (18) into (21) and splitting the sum into two parts, following Doviak and Zrnić (1984, §4.1), gives

$$P_r(t) = \sum_{m,n} A_m A_n^* \exp[i(\omega_m - \omega_n)t] \exp[-2i(k_m r_m - k_n r_n)], \quad (22)$$

$$= \sum_m A_m A_m^* + \sum_{m,n,m \neq n} A_m A_n \exp[i(\omega_m - \omega_n)t] \exp[-2i(k_m r_m - k_n r_n)], \quad (23)$$

where $k_m \equiv \omega_m/c$. Arguments for using only the *first term* in (23) in order to evaluate reflectivity, i.e., for summing the powers received from each droplet, are given by Rayleigh (1945, p. 37), Beckmann (1962), and Doviak and Zrnić (1984, §4.1). The important point, which was phrased eloquently by Rayleigh, is that it is not correct to say that the power in a single return from a random distribution of droplets is the sum of the powers scattered by each. Rather, the result is true only when a *large ensemble of returns* from a statistically stationary target are averaged. This is most easily seen when we consider the case when all the A_m are equal (to unity, say). Then, the first term T_1 in (23) is $T_1 = N_d$. If droplet distances are randomly distributed in the resolution shell (assumed to be several wavelengths wide), then the magnitude of the second term will be the average of the summands times the number of terms, i.e., $T_2 \approx N_t^{-1/2} \times N_t = N_t^{1/2} \approx N_d$, where $N_t = N_d(N_d - 1)$ is the number of terms in the double sum. Hence both terms in (23) are of *similar*

331 *magnitude*. To make the second term smaller than the first, an ensemble average must be taken
 332 over many pulses. If the ensemble has N_s phase-uncorrelated samples, then the second term will
 333 be $N_s^{1/2}$ smaller than the first.

334 In the present application, the wake descends through the beam and so the target is not stationary,
 335 strictly speaking. In §3d we will explicitly verify that, for our case, an average of (22) over a certain
 336 number of pulses does indeed yield the first term in (23). Note that a radar set does not have direct
 337 access to the first term in (23); only we as simulators do.

338 To provide a measure of detectability, we will present the signal-to-noise ratio

$$\text{SNR1} \equiv P_{r1}/P_{\text{noise}}, \quad (24)$$

339 where P_{r1} is the first term in (23) and the average noise power is

$$P_{\text{noise}} = k_B T_0 F_N / \tau, \quad (25)$$

340 where $k_B = 1.381 \times 10^{-23} \text{ J K}^{-1}$ is Boltzmann's constant, $T_0 = 290 \text{ K}$ is a reference temperature
 341 set by convention, and F_N is the overall noise figure of the chain of components in the receiving
 342 cascade. Values for F_N and τ are listed in Table 4 for each radar set.

343 Finally, since each computational droplet represents a multiplicity M_{actual} of actual droplets, we
 344 have

$$\sum_{m=1}^{N_d} \rightarrow M_{\text{actual}} \sum_{m=1}^{N_{\text{comp}}}, \quad (26)$$

345 where N_{comp} is the number of computational droplets in the resolution volume. Note that all M_{actual}
 346 copies of each computational droplet are assumed to be at the same location and therefore their
 347 scattered voltages at the receiver add constructively. This assumption does not bias SNR1 since
 348 its calculation involves summing individual scattered powers anyway. We claim that the statistics
 349 of individual pulse returns are also not affected by this assumption; this will be verified (§3e) in a
 350 computational test where the number of computational droplets is increased.

h. Calculation of the doppler spectrum

Radars calculate a doppler spectrum for a given spatial observation location by performing a Fast Fourier Transform (FFT) of complex voltage returns (at the same range gate) from a sequence of pulses separated by $\Delta t_{\text{pulses}} = 1/\text{PRF}$, where PRF is the pulse repetition frequency. We shall do the same for the simulations. From a series of pulse returns, V_n , $n = 0, 1, \dots, N_{\text{FFT}} - 1$, the normalized transform

$$\hat{V}(k) \equiv \frac{1}{N_{\text{FFT}}} \sum_{n=0}^{N_{\text{FFT}}-1} V_n e^{-i2\pi kn/N_{\text{FFT}}}, \quad k = 0, \dots, N_{\text{FFT}} - 1, \quad (27)$$

and then the power spectrum $S(k) \equiv \hat{V}(k)\hat{V}^*(k)$ is computed. Note that the frequency index k corresponds to an actual frequency

$$k_{\text{actual}} = \begin{cases} k, & k \leq N_{\text{FFT}}/2; \\ k - N_{\text{FFT}}, & N_{\text{FFT}}/2 < k \leq N_{\text{FFT}} - 1. \end{cases} \quad (28)$$

The frequency k_{actual} is in units of (the period of the sequence) $^{-1} = (N_{\text{FFT}}\Delta t_{\text{pulses}})^{-1}$, so in units of s^{-1}

$$f(k_{\text{actual}}) = \text{PRF } k_{\text{actual}}/N_{\text{FFT}}. \quad (29)$$

Equating this to $-2(u_{\text{doppler}}/c)f$ gives the doppler velocity associated with each k_{actual} . Finally, we state that we use the Hamming window (e.g., Harris 1978).

i. Antenna gain function

We assume a Gaussian beam with transmitted power flux (power per unit area) vector

$$\mathbf{S}_t = A \exp(-\theta^2/\theta_0^2) \hat{\mathbf{r}}, \quad (30)$$

where A is a coefficient, θ is the angle from the beam centerline, and

$$\theta_0 = \left(2\sqrt{\ln 2}\right)^{-1} \theta_b \quad (31)$$

in terms of the half-power full-width, θ_b . The total power crossing a sphere of radius r is

$$P_t = 4\pi r^2 \int_0^\pi \mathbf{S}_t \cdot \hat{\mathbf{r}} \sin \theta, d\theta = 2\pi r^2 \theta_0^2 A, \quad (32)$$

for a narrow beam. Using the definition of the gain function, $G(\theta)$, we obtain

$$G(\theta) \equiv \frac{4\pi r^2 S_t}{P_t} = \frac{2}{\theta_0^2} \exp(-\theta^2/\theta_0^2) \quad (33)$$

j. Radars included in the study

Table 4 lists parameters of currently operational ground-based doppler weather/cloud radars considered in the present study. The S, C, and X-band radars chosen are the DWSR series manufactured by EEC (Enterprise Electronics Corporation, Enterprise, Alabama). ARC (Advanced Radar Corporation, Boulder, Co.) makes quite similar C and X-band radars, while Baron Services (Huntsville, Al.) makes similar S, C, and X-band radars. The power and beamwidth values of the C-Band TDWR (Terminal Doppler Weather Radar) deployed at many US airports is subsumed by the range of values provided by the EEC C-band radar, and is therefore not included here.

A number of descriptions of Ka-band (35 GHz) cloud radars have appeared in the literature (Hamazu et al. 2003; Görsdorf et al. 2015). In the present work, we use parameters of the MIRA-35 radar manufactured by Metek (Elmshorn, Germany) which is described in Görsdorf et al. (2015). This choice was motivated by its relatively high power (30 kW). Other Ka-band weather radars, operational at the time of writing are: (i) Scanning 2 kW radars operated by U.S. Department of Energy's Atmospheric Radiation Measurement (ARM) Climate Research Facility (Widener et al. 2012). (ii) The Copernicus 1 kW radar at Chilbolton Observatory (UK). (iii) An airborne 25 kW multi-frequency (X, Ka, and W-band) radar developed by Prosensing that is being used by NASA's Langley Research Center for research into the detection and avoidance of super-cooled water droplets.

386 The science and technology of W-band (94 GHz) radars for cloud and precipitation research is
 387 reviewed in Kollias et al. (2007). For the present work we chose the W-SACR radar, which has
 388 been developed by the U.S. Department of Energy’s Atmospheric Radiation Measurement (ARM)
 389 program (Widener et al. 2012; Kollias et al. 2014).

390 With increasing frequency, f , reflectivity increases as f^4 in Rayleigh’s formula (ignoring
 391 Mie-scattering corrections). Furthermore, the size of the antenna required to obtain the same
 392 beamwidth is reduced. The main drawback of high frequency is increased attenuation due to pre-
 393 cipitation between the radar and target. For example, the last entry in Table 4 gives the attenuation
 394 rate in medium rain at W-band as 7 dB/km. A compensating factor is that when there is precipi-
 395 tation, the ambient humidity is also very high and so there is minimal evaporation, and, if natural
 396 precipitation is present in the wake, it will also contribute to reflectivity.

397 *k. Mie cross-section and phase-shift*

398 Since we have can rather large droplets in the present application and frequencies up to 94
 399 GHz, the back-scattering cross-section and phase-shift are obtained using Mie’s formula instead
 400 of Rayleigh’s approximation. We used subroutine BHMIE, available from Prof. B.T. Draine’s
 401 website at Princeton University, and checked the results using subroutine MIEV0 developed by
 402 Dr. W.J. Wiscombe (NASA Goddard).

403 Some understanding of notation is required to properly use these routines. Let the incident field
 404 be of unit magnitude and polarized in the 2-direction (defined to be perpendicular to the plane
 405 containing the incident and observer directions). For a spherical target, the scattered field in the
 406 far-field is also polarized in the 2-direction and is given by

$$E_{s2}(r, \theta) = \frac{e^{ikr}}{kr} f_{22}(\vartheta), \quad (34)$$

where f_{22} is complex, $k = 2\pi/\lambda$, ϑ is the angle of the observer relative to the direction of propagation of the incident wave, and r is distance from the center of the sphere. The backscattering cross-section and phase shift are obtained as

$$\sigma_b \equiv 4\pi r^2 \frac{|\mathbf{E}_s(\pi)|^2}{|\mathbf{E}_i|^2} = \frac{4\pi}{k^2} |f_{22}(\pi)|^2, \quad (35)$$

$$\phi = \arg(f_{22}(\pi)). \quad (36)$$

At the start of the reflectivity calculation at a given frequency, we tabulate the ratio $\sigma_b/\sigma_{b,\text{Rayleigh}}$ and the difference $\phi - \phi_{\text{Rayleigh}}$ as a function of droplet radius a . Rayleigh's formulas are (Ishimaru 1978, p. 19)

$$\sigma_{b,\text{Rayleigh}} = 4|K_\varepsilon|^2 (ka)^4 (\pi a^2), \quad (37)$$

$$\phi_{\text{Rayleigh}} = \arg(K_\varepsilon), \quad (38)$$

where K_ε (a complex number) is given by

$$K_\varepsilon = \frac{\varepsilon - 1}{\varepsilon + 2}. \quad (39)$$

The quantity $\varepsilon(f, T)$ is the complex dielectric constant of water; our convention of $e^{+i\omega t}$ for the time dependence requires the imaginary part of ε be positive for an absorbing material. It is a function of frequency and temperature and was evaluated using the single Debye model of Liebe et al. (1991) as implemented in subroutines available from Prof. Chris O'Dell's website at Colorado State University. Since the droplet temperature is almost the same for all drops (the spread was 4 C at most), the dielectric constant ε is evaluated at the average temperature of all the drops in the trail.

Figure 2 displays the Mie back-scattering cross-section σ_b (normalized by the Rayleigh value) and phase-shift ϕ as a function of droplet radius at the five frequencies considered in this work.

At the largest radii in this work, $a \approx 600 \mu\text{m}$, the error in using Rayleigh's cross-section is about 20% at 35.1 GHz.

l. Choice of ambient temperature and humidity

Droplet evaporation calculations require specification of the ambient temperature and humidity. For guidance on appropriate choices, METARs (Meteorological Aerodrome Reports) during 2000-2014 were downloaded from

<http://mesonet.agron.iastate.edu/request/download.phtml>

and processed for the five busiest airports in the U.S. Figures 3a and b show the monthly-averaged temperature and relative humidity (RH), respectively, when IFR conditions prevailed. Figure 3c shows the percentage of reports that fall into the IFR category. One sees that the average RH is always above 90%. To further synthesize this data, yearly averages were taken (Table 5). Among the five airports, LAX has the highest rate of evaporation in IFR conditions on average since it is the warmest and driest on average. Our choice is the IFR average for LAX, namely, $T = 15.2$ C and $\text{RH} = 92.7\%$. Looking at the monthly data for the other four airports, this appears to be a reasonable choice for them also: it is an approximate lower bound for their monthly RH and their temperature is higher only during the summer months when IFR reports are low.

Since it is expensive for flight tests to wait for IFR conditions to occur, and it is desirable to have a wake sensor that can work in a wider variety of atmosphere conditions, we will also consider a case of lower humidity and higher temperature, namely, $\text{RH} = 60\%$ and $T = 20$ C.

m. Radar placement with respect to the wake

Here, we choose the radar location $(x_{\text{rad}}, y_{\text{rad}}, z_{\text{rad}})$ in aircraft-centered coordinates. Based on current wake separations (Table 1), it should not be necessary to examine a wake more than 6 nm

445 behind the aircraft. We therefore chose to present results for the reflectivity at $x = 6$ nm, the worst
 446 case for droplet loss by evaporation and sedimentation. The radar is also placed at on the ground at
 447 $x_{\text{rad}} = 6$ nm so it can view the $x = 6$ nm wake cross-section at normal incidence. Next, we assume
 448 that the aircraft is at the touchdown point. At 6 nm from the touchdown point, the altitude of an
 449 aircraft flying a 3° glide slope is $H = 582$ m. Therefore, the vertical coordinate of the radar is
 450 $z_{\text{rad}} = -582$ m. For purposes of this study, we assume an aircraft flying straight and level at this
 451 altitude. Initial flight tests would also presumably have the aircraft fly straight and level. In this
 452 case, since the vortex pair descends at a speed of $W_{\text{desc}} = 1.75 \text{ m s}^{-1}$, its axis makes a downward
 453 angle of 1.7° relative to the horizontal. For an aircraft on a 3° glideslope, the vortex axis would
 454 therefore be 1.3° upward from the wing. This difference in the angle of the wake axis is expected
 455 to have a very small effect on reflectivity.

456 To place the radar laterally with respect to the wake, we imagine several parallel approaches that
 457 are monitored by the same radar. The largest separation between parallel runways is about 5000
 458 ft (Doyle and McGee 1998). At 6 nm from touchdown, the lateral width of the ILS (Instrument
 459 Landing System) approach is 3182 ft for a standard 5° splay, and we imagine an aircraft that has
 460 strayed to the outer edge of this zone. If the radar is placed in the middle of the two furthest
 461 runways we obtain a lateral distance of 0.67 nm. In the presence of a crosswind, we imagine that
 462 the wake would be monitored for as long as it remained between the outer edges of the left and
 463 right ILS zones. In conclusion, we select $(x_{\text{rad}}, y_{\text{rad}}, z_{\text{rad}}) = (6 \text{ nm}, -0.67 \text{ nm}, -582 \text{ m})$ relative to
 464 the aircraft.

465 The elevation angle of the radar beam from this location varies between 10.6° and 17.1° as the
 466 scanned range of z on the wake center plane varies between $z = -350$ and -200 m (see Figure 4).
 467 Since the beamwidth of the radar likely to be used is $\leq 1^\circ$, ground reflection will be small. To
 468 significantly reduce ground and structure clutter, the radar can be placed directly under the flight

469 path. This would require a separate radar for each parallel runway. Another issue is loss of radar
 470 sensitivity at smaller ranges; for MIRA-35 this happens for $r < 360$ m (Matthias Bauer-Pfundstein,
 471 private communication). However, this loss is probably offset by the increase in power from the
 472 r^4 factor in Equation (20).

473 3. Results

474 a. Signal-to-noise ratio for the IFR case

475 We begin by considering IFR ambient conditions ($RH = 92.7\%$, $T = 15.2$ C) chosen as described
 476 in §2l. Nozzle 1 from Table 2 is used and parameters for the injected square of droplets, described
 477 in §2e, are $n_{\text{square}} = 15$, $n_x = 120$, and $w_{\text{square}} = 1$ m. Figure 4 shows simulated values of SNR1,
 478 calculated using (24), for the five radars listed in Table 4. Each SNR1 plot is an instantaneous
 479 range-elevation scan of the $x = 6$ nm cross-section of the wake and each location on the plot corre-
 480 sponds to the mid-radius of a resolution shell along the beam centerline. The pulse width is chosen
 481 to be $\tau = 0.2 \mu\text{s}$ for all the radars except for DWSR-8501S, in which case the lowest available τ of
 482 $0.4 \mu\text{s}$ is used. Droplets in a 30 m thick axial slab centered at $x = 6$ nm are shown in panel (a). Due
 483 to centrifugation, larger droplets lie at greater distances from the vortex center, which is devoid of
 484 droplets. The very large particles sediment due to gravity after being centrifuged. Except for the
 485 S-band radar, all radars give $\text{SNR1} > 10$ dB at most points surrounding the vortices; the reflectivity
 486 is higher for the higher frequency radars. The W-SACR radar gives the highest reflectivity despite
 487 having the smallest pulse power.

488 For all radars, there is a drop in reflectivity near the 2 o'clock and 4 o'clock positions for the
 489 left vortex (8 and 10 o'clock positions for the right vortex). This manifests as a crescent-wrench
 490 shaped reflectivity pattern that is most prominent for the DWSR 2001X radar. A plot of droplet

491 number density indicated a drop at these locations. How this is related to the vortex flowfield,
 492 remains to be elucidated.

493 *b. Effect of pulse width and beam width*

494 Consider a distribution of droplets that is homogeneous in the range of pulse volumes (resolution
 495 length \times beam section) considered. Then, from Equation (20) the dependence of received power
 496 (P_r) on pulse width (τ) and beam width (θ_b) is

$$P_r \propto (R\theta_b)^2 (c\tau/2) G^2 \propto \tau \theta_b^{-2}, \quad (40)$$

497 since the antenna gain $G \propto \theta_b^{-2}$. Figure 5a shows the effect of using the four times smaller pulse
 498 width of $\tau = 0.05 \mu s$ available in the W-SACR radar; compare this with Figure 4f. One sees that
 499 some of the spiral structure of the droplet pattern is now resolved at the expense of a 6 dB drop
 500 in SNR1; this is in accordance with (40). Figure 5b shows the difference in SNR1 (dB) when
 501 the $\theta_b = 0.31^\circ$ beam is used for the Mira-35 radar instead of the $\theta_b = 0.52^\circ$ beam. The observed
 502 difference agrees approximately with the difference of 4.5 dB given by (40). Locations where the
 503 difference does not equal this value are those where the droplet distribution is not homogeneous.

504 *c. Insensitivity to initial condition*

505 To test sensitivity to initial conditions, instead of injecting droplets in a regular grid pattern
 506 on each square, droplets were randomly placed in the squares. Figures 6a and b show that both
 507 the droplet configuration at $x = 6$ nm as well SNR1 for DWSR-2001X are changed very little;
 508 compare with Figures 4a and d. We expect this to be true for all the radars as well. In another test
 509 (Figure 6c and d), the width of the square, w_{square} , was reduced from 1 m to 50 cm, keeping the
 510 number of droplets fixed. This increases the initial number density in the cross-plane (yz) and, to
 511 keep the spacing the same in the streamwise (x) direction, the injection interval Δt_{inject} was also

512 halved. One might think that this would increase the number density downstream. However, the
513 flow tends to both reduce number density (where there is rotation) and increase it (where there
514 is strain), and eventually, the number density tends to a distribution that is mostly independent of
515 initial condition.

516 *d. Pulse to pulse fluctuation and averaging*

517 The SNR1 results in §3a were based on using the first term in Equation (23), which sums the
518 powers reflected by individual droplets. It was argued that for a statistically stationary target, this
519 should equal the average power from many pulses. In the present case, the droplet configuration
520 is not spatially homogeneous and is descending through a fixed beam. Hence, the question arises
521 whether the powers returned from a sequence of pulses can be considered to be statistically sta-
522 tionary in a certain interval, and if so, how many pulses is sufficient to recover the SNR1 values
523 presented.

524 To obtain complex voltage returns from a sequence of pulses one needs to evolve the wake in
525 time, however, the method that was described in §2 gives a trail of droplets at a single instant of
526 time, t . To evolve this configuration to time $t + \Delta t$, the configuration at t is translated horizontally
527 by $\Delta x = -U_{\text{app}}\Delta t$, i.e., the droplet trail is assumed to be invariant in a reference frame moving to
528 the left with the airplane. This procedure does not correspond exactly to reality, but captures both
529 the rotation of droplets around the vortices, and their vertical descent with time at a fixed location.
530 The received complex voltage is evaluated using (18) at a sequence of times separated by the pulse
531 repetition period, keeping the resolution volume centered at $(x, y, z) = (6 \text{ nm}, -50 \text{ m}, -230 \text{ m})$.
532 This location corresponds to the upper SNR1 peak of the crescent wrench in Figure 4. The value
533 of the pulse repetition frequency (PRF) was chosen to be at or close to the highest value available
534 for each radar.

Figure 7 shows the result for a time period during which a cluster of droplets enters and leaves the beam. To save space, plots for the S and C-band radars have been omitted; they tell the same story. The power in individual pulse returns is shown in gray. The total number of active pulses changes from radar to radar because their beam widths and PRFs are different. In particular, the period of activity was found to equal the time it would take the vortex pair to descend through roughly one-third of the vertical projection of the half-power beam width. The average of pulse powers is shown in green over an averaging segment whose length is 512 pulses. The red curve shows the value of SNR1. Our assumption was that SNR1 (red) should equal the green level. This is seen to be true to a good degree. The fluctuations are due to statistical error and were found to decrease with increasing the averaging interval. It is worth remembering here that the radar has access to only the individual pulse returns and their average (for example the green values); only the simulation has access to the red curve (SNR1).

e. *Convergence of pulse statistics*

Recall that each computational droplet at a single location represents M_{true} actual droplets located at different positions; in fact $M_{\text{true}} \approx 100$ in the calculations presented. It was claimed (§2g) that this should not affect pulse statistics, provided the number of computational droplets is sufficiently large. To verify this, the number of computational droplets was increased by four. Random placement of droplets was employed in the injected squares. Four realizations of the droplet trail were generated using different random number seeds for the initial size distribution and droplet placement. The four realizations were then merged into one trail for the radar reflectivity calculation. Figure 8 shows that the probability density $p(|V|)$ of the modulus $|V|$ of complex voltage is unchanged by the resolution refinement. The probability densities are very well fit by the Rayleigh

distribution (Beckmann 1962)

$$p(|V|) = \frac{|V|}{\sigma_R^2} \exp(-|V|^2/2\sigma_R^2), \quad (41)$$

having the same mean as the data. The Rayleigh distribution results when the scattering amplitude is the same for all droplets and the phases uniformly distributed. The case selected is the same as that shown in Figure 7d (apart from the random placement of droplets in the injected squares). Pulses in the interval of stationarity were chosen, namely pulse number $\in [-8000, 8000]$.

f. A non-IFR condition

It would be valuable to have the capability to detect wakes in non-IFR conditions. Furthermore, in a flight test study of the feasibility of the present proposal, it would be too costly to wait until IFR conditions occur before a test can be conducted. For this reason it is of interest to know what reflectivity is obtained at less humid and less cold conditions. We chose $RH = 60\%$ and $T = 20\text{ C}$.

With the previous choice of $n_{\text{square}} = 15$ and $n_x = 120$ as injection parameters, it was found that a high rate of evaporation resulted in a small number of computational droplets remaining near $x = 6\text{ nm}$. This increased statistical error. To reduce sampling error, an ensemble of ten trails were computed with different random number seeds for the droplet size sample. The ensemble was then combined into a single trail for the reflectivity analysis. As a result, the total number of computational droplets is so large that each one presents only 9.8 true droplets in the reflectivity analysis.

Figure 9 shows that only the high-frequency radars, MIRA-35 and W-SACR, give positive values of SNR1 (dB) in the vicinity of the vortices, and even these values are marginal. To increase SNR1, the number of nozzles could be increased; for instance four nozzles on each side of the aircraft would increase SNR1 by 6 dB.

578 There is a powerful method that enables detection even when $\text{SNR1 (dB)} < 0$. It comes at the
579 cost of increased dwell and processing time. We learnt about the method from notes on the sen-
580 sitivity of the MIRA-35 radar given to us by Matthias Bauer-Pfundstein (Metek). It is also briefly
581 described in Görsdorf et al. (2015, p 680). The idea is that in a discrete Fourier transform, the
582 noise is spread equally to all the frequency bins, whereas the spectrum of the signal is confined to
583 only a few of the bins. (The latter is true provided the probability distribution of droplet velocities
584 in the resolution cell is narrow compared to $2U_{\text{max}}$ for the radar. For MIRA- 35, for example, at
585 $\text{PRF} = 10 \text{ kHz}$ we have $2U_{\text{max}} = 42 \text{ m s}^{-1}$ and so this is unlikely to be an issue.) Hence, an FFT
586 effectively reduces the noise by a factor of N_{FFT} .

587 To investigate this technique, complex (Gaussian distributed) white noise with a mean power
588 equal to P_{noise} for the radar was added to complex voltages of pulse returns. Illustrative results
589 are shown in Figure 10 for $N_{\text{FFT}} = 512$. Panels (a) and (b) are for a range cell centered at the
590 left white dot in Figure 9e where $\text{SNR1} = -2.7 \text{ dB}$. Panels (c) and (d) are for the right white dot
591 where SNR1 is even lower, namely, -7.2 dB . Consider panels (a) and (b). An averaging of pulse
592 power returns by the radar would give values (the green line) only slightly above the noise, not
593 enough for a positive detection. Averaging the doppler spectra from 10 segments gives panel (b)
594 with a peak 40 dB above the noise. In the present example, this would require a dwell time of 0.5
595 s for each elevation angle. For the second location where SNR1 is weaker, the doppler spectrum
596 has a peak that is about 25 dB above the noise (using the same dwell time). The contribution
597 to the doppler spectra from noise can be estimated as $P_{\text{noise}} \sigma_{\text{win}}^2 / N_{\text{FFT}} = -162 \text{ dB Watts}$, where
598 $P_{\text{noise}} = 8.34 \times 10^{-14} \text{ Watts}$ is the average noise power for the Mira-35 radar and $\sigma_{\text{win}}^2 = 0.397$ is
599 the mean-square of the Hamming window.

600 *g. Power-weighted average radial velocity*

601 It has been stated (Doviak and Zrnić 1984, §5.2) that the first moment of the doppler spectrum is
602 the radial velocity of droplets in the resolution volume, weighted by their individual scattered pow-
603 ers. This is reasonable although we have neither encountered nor attempted a proof of it starting
604 from Equation (22). Figure 11 displays the power-weighted average radial velocity correspond-
605 ing to the cases previously shown in Figure 4. Only points where SNR (dB) > 0 are shown. The
606 actual radial velocity (with respect to the radar) of the gas is shown in panel (f). The radar data
607 appears as a filtered version of the actual velocity and, due to particle centrifugation, is unable to
608 detect the maximum value of 19.8 m s^{-1} in the vortex core. Nevertheless, the radars give a good
609 representation of the gas velocity where particles are present. To estimate vortex circulation, the
610 observed velocity is multiplied by $2\pi r$ where r is the distance from the vortex center and can be
611 determined from the location of zero radial velocity.

612 *h. Comparison of four nozzles*

613 Finally, Table 6 compares SNR1 reflectivity for the four nozzles listed in Table 2. The range
614 cell for all cases is centered at $(x, y, z) = (6\text{m}, -50\text{m}, -230\text{m})$, which corresponds to the top of
615 the crescent wrench in Figure 4. IFR ambient conditions have been assumed. It is observed that
616 the quantity $\dot{\zeta}_{\text{nozzle}}^<$ (defined in Equation 9), which depends only on the droplet size distribution
617 produced by a nozzle, provides an excellent indicator of the relative performance of different
618 nozzles.

619 To provide further insight we compute the quantity ζ_x which is defined to be ζ (see Equation
620 8) per unit axial length of the wake. It is calculated as a diagnostic of the droplet trajectory and
621 size evolution and is shown in Figure 12. The solid lines give the total value (over an entire cross-
622 section) and diagnose total evaporative loss. The dashed lines give the contribution from droplets

in a neighborhood (defined in the caption) of the vortex: these curves diagnose both evaporative loss and loss by sedimentation. The ordering of ζ_x values (pertaining to the neighborhood of the vortex) at $x = 6$ nm, which are also listed in the last column of Table 6, matches the ordering of SNR1 for the different nozzles.

All statements of comparison in the following are relative to nozzle 1 and make reference to Figure 12a. If the increased SNR1 reflectivity of nozzle 2 were due to increased volume alone, we would get a 2.4 dB increase in reflectivity. The actual increase is 1.03 dB. To understand this, we first observe that nozzle 2 (solid red line) initially has a 0.7 dB higher value of ζ_x , less than the 2.4 dB increase in its volume flow-rate. This is because nozzle 2 produces more small droplets. By $x = 6$ nm the 0.7 dB increase has been reduced to 0.55 dB because the smaller droplets of nozzle 2 evaporate faster. The fact that ζ_x in the vicinity of the vortex is 0.6 dB higher must arise from the fact that the smaller droplets of nozzle 2 have sedimented less.

Consider nozzle 3 (green curves). If its smaller reflectivity (relative to nozzle 1) were due to decrease in volume, then we would expect a -0.91 drop in SNR1 which is close to what is obtained. This is understandable given that its initial ζ_x is very nearly the same as for nozzle 1. This is surprising given that nozzle 3 has many more smaller droplets. However, close inspection of its size distribution (green line in Figure 12b) shows that it also has more droplets that are very large (specifically $a > 370$ μm). This fact also explains the more rapid loss of ζ_x by sedimentation (dashed green curve in Figure 12a) and less rapid loss by evaporation (solid green curve). Overall, these two effects balance and the final effect that remains is that due to volume decrease.

Despite its smaller flow-rate, nozzle 4 has a higher initial value of ζ_x ; see the solid blue curve. This is because it produces more large droplets. Unfortunately, they rapidly fall out of the wake (dashed blue curve).

i. Azimuthal scanning

Instead of having a few radars at different axial locations, all pointing at the wake at normal incidence, it would be cheaper for a single radar to azimuthally scan a wake. Figure 13 shows SNR1 for a Mira-35 radar located at $x_{\text{rad}} = 4$ nm which observes the wake at azimuthal angles of -71.5° , 0° , and 71.5° measured clockwise from normal incidence. Note that the results are presented in the cross-sectional plane of the aircraft rather than in the scanning plane. For these angles, the wake center is located at $x = 2, 4$, and 6 nm miles behind the aircraft, respectively. The wake is detectable at all three angles, although marginally so for the most downstream scanning plane.

4. Concluding Remarks

It was proposed that spraying a small amount of water into the vortex wake of a heavy aircraft during landing can make the wake visible to existing weather/cloud radars and thereby aid air traffic controllers in selecting appropriate aircraft separations. This approach could also be used for wake vortex studies of aircraft.

Simulations of the radar reflectivity of the spray trail were performed for existing weather/cloud radars. For ambient humidity at the lower end of values typical for IFR conditions, the results showed that that good signal-to-noise (SNR) ratios (averaged over many pulses) are obtained at distances behind the aircraft of up to 6 nm, the largest that would be contemplated given existing wake separations used in air traffic control. For the case most studied here, the amount of water spray was 3 gallons per nautical mile of wake that needs to be detected. A currently available nozzle used for agricultural spraying can be used. A doubling of volume by doubling the number of nozzles gives a proportional increase in SNR. For a case of average humidity, evaporation for severe and pulse-averaged, SNR values dropped below unity. However, since the pulse returns of

669 the wake remained statistically stationary for 1 to 6 secs (depending on the radar), it was shown that
670 the signal-to-noise ratio can be increased to detectable levels by spectral (doppler) processing and
671 averaging doppler spectra for consecutive time segments. This would require greater dwell time
672 for each direction the radar is pointed at. Ultimately, selecting the dwell time for a given situation
673 will be a trade-off between quickly completing a scan of a wake cross-section and increasing SNR.

674 1. Suggested future work

675 (a) As an airplane nears the touch-down point, flaps are deflected at increasing angles. The
676 presence of flap vortices should be included in future analysis.

677 (b) The present work has ignored space-time fluctuations of the air velocity field. They will
678 arise from the direct effect of atmospheric turbulence and from vortex core waviness
679 induced by atmospheric turbulence, and further amplified by vortex core instabilities.
680 Velocity fluctuations will disperse the spray trail and if this happens on the scale of
681 the pulse width or beam width, then reflectivity will be reduced. This effect should be
682 studied in subsequent work.

683 (c) There are two fluid mechanical issues which we believe are of lesser importance to the
684 proposed concept than those listed above. They are unlikely to be resolved soon but
685 should be kept in mind and considered to the extent possible. These are growth of the
686 vortex core size due to small-scale turbulence internal to or near the vortex core, and the
687 loss in circulation due to mutual annihilation.

688 (d) The issue of droplet coagulation was raised by the second referee. An upper bound
689 on the rate of coagulation is provided in §C of the online Supplemental Materials with
690 the conclusion that, while coagulation should be included in future work, its effect on
691 reflectivity is not catastrophic.

(e) The first referee raised the issue of cost. The only price we were provided and allowed to quote is that of Mira-35, which is about 0.5M Euros. The most expensive items in a radar system are the antenna pedestal and the power source; their price scales with size and power, respectively. We begin by excluding S and C-band radars relative to X-band due to the latter's smaller antenna size and higher reflectivity for the same peak power (and therefore possibly the same cost). James Mead of ProSensing suggested that the required power could be reduced by using spectral processing together with pulse compression, using a linear FM pulse, for instance. For example, with $N_{\text{FFT}} = 128$ and a pulse compression factor of 10, the required power would be reduced by a factor of 1280. Scaling the peak powers in Table 4 by this factor suggests that a solid-state power amplifier (SSPA) with 150 Watts of peak power could then be used at X-band or 25 Watts at Ka band. The cost of SSPAs increases with frequency, however, this might be offset by the reduced cost of the antenna pedestal with increasing frequency. One advantage of an SSPA is high duty cycle which allows high pulse rates and therefore coherent processing to increase SNR. This assumes that the CPU can keep up with the data rate. This and other ideas for cost reduction should be investigated.

(f) Consideration should be given in the future to real-time scanning and processing. For instance, how long it would take for a single radar to complete a scan of all the approach paths?

(g) Airborne weather radar, which usually operates in the X-band, was enhanced in the 1990's to detect wind shear. Section E in the online Supplemental Materials shows that in order to detect a spray trail, the sensitivity of such radars needs to be improved by between 26 and 40 dB.

2. Application notes

(a) For the purposes of simulation we generated a spray trail that was 7 nm long. In practice, to reduce the volume of water, spray could be released only at a few axial locations where a detection would be performed. For each detection location, the length of the trail would need to be a few beam widths long and the release location would have to account for any head/tail wind. A trail segment that is three full beam widths long would be 0.06 nm long and this would require only 0.17 gallons. This value assumes that $\theta_b = 1^\circ$, range = 1 km, and a flow-rate of 3 gallons nm^{-1} (counting both sides of the airplane). Hence, there is considerable room for increasing water volume, and therefore signal-to-noise ratio. The main difficulty is that for the nozzles presently considered, more than one would be required for increased flow-rate. A better solution might be to design a spray head containing several nozzles.

(b) Short trail segments would be difficult for the radar to find, particularly in the presence of wind drift and other perturbations. A continuous trail might therefore be required. In this case the total volume of water would be 18 gallons for a 6 nm-long trail; this introduces a 150 pound weight penalty. The cost of this would have to be traded-off against gains in airport capacity.

(c) Given that spectral processing is required for detection in conditions of average humidity, it is likely that processing decisions will have to be based on humidity or on the quality of incoming returns. If the humidity is high and the quality of returns high, then the mean velocity can be obtained from a pulse-pair estimate. If the humidity is low, then spectral processing can be turned on.

- (d) Some of the requirements of the present application are similar to those for radar imaging of tornados (French et al. 2014). This includes a smaller detection volume and the need to complete a scan faster than the vortex evolution time. Therefore, technology developed for that application could be useful here.
- (e) In IFR conditions, natural precipitation (fog, mist, drizzle, or heavy rain) will be present between the radar and the wake and lead to absorption. However, at ranges of ≈ 1 nm envisioned for the present application, this is small.
- (f) If spraying is to be employed in very cold conditions (Denver, Colorado comes to mind), freezing of water must obviously be prevented in the water storage and delivery system.
- (g) Several US airports have approaches that are over water which would make it difficult or impossible to implement the proposed system. Such airports include Boston-Logan, San Francisco, St. Pete-Clearwater, New Orleans-Lakefront, and Portland, Maine.
- (h) *Dual polarization.* Droplets moving relative to the air become oblate due to a higher air pressure at the front stagnation point and low pressure at 90° from the front stagnation point. For falling rain droplets, this results in greater reflected power from incident waves that are horizontally versus vertically polarized (Doviak and Zrnić 1984, §8.5.3). Most weather radars employ dual polarization to obtain more information about rainfall rate. Since, in the present case, droplets revolving around the vortices are small and their velocity relative to the air is also small, we expect that droplets will remain very nearly spherical. Therefore, it is not expected that dual polarization would provide additional information about the flow. However Keränen and Chandrasekhar (2014) have suggested that dual polarization could be used for enhancing SNR. This works by exploiting coherence between signals in the horizontal and vertical channels.

- (i) Since the maximum range pertinent to the present application is much lower than for cloud and precipitation detection, the pulse repetition frequency could be increased (the maximum duty cycle of the klystron or magnetron permitting) in order to reduce the dwell time for spectral averaging.
- (j) One obvious modification of existing cloud/precipitation radar software for the present application would be a reduction in the spacing of range gates from their current values, for example 25 m which is employed in Ka-SACR and W-SACR (Kollias et al. 2014).
- (k) Another possibility for radar placement is under the flight path. This reduces the range and therefore increases reflectivity, however, it necessitates separate radars for each approach path. With reduced range, consideration must be given to the minimum range of the radar. For the Mira-35, the minimum range is 150 m which arises due to the switching delay of the transmit-receive switch. This value is constrained not only by switching technology but also by the need to protect the receiver from an unexpected strong reflector nearby, such as an airplane.

Acknowledgments. I am grateful to several individuals for sending me information when requested and sometimes more information than requested. Matthias Bauer-Pfundstein (Metek) sent me information on the MIRA-35 radar including a detailed dBZ sensitivity calculation, information on signal processing, and detailed information on loss determination. It was from his dBZ sensitivity document that I learnt that a discrete Fourier transform enhances signal-to-noise ratio in the spectral bin of interest. John Cho (MIT Lincoln Laboratories) sent me information on the TDWR (Terminal Doppler Weather Radar). Brad Fritz (U.S. Dept. of Agriculture) sent me his Excel program giving parameters of the droplet size distribution produced by different aerial spray nozzles at different free-stream air speeds. He also experimentally measured for me the flowrate

783 of the Davidon-Triset nozzle. Calvin Kroes (CP Products) sent me information on nozzle orifice
784 areas, flow rates, and exit velocities for various CP nozzles. Keith Vickers (Enterprise Electronics
785 Corporation) sent me basic information on the DWSR series of radars. Dr. James Mead (ProS-
786 ensing Inc.) provided some useful cost reduction suggestions. I am grateful to Alan Wray (NASA
787 Ames) for useful discussions. I am grateful to Jasim Ahmed and Alan Wray for performing the
788 internal review and to the external reviewers for their useful suggestions.

789 **References**

790 Apte, S., M. Gorokhovski, and P. Moin, 2003: LES of atomizing spray with stochastic modeling
791 of secondary breakup. *Intl. J. Multiphase Flow*, **29**, 1503–1522, doi:10.1016/S0301-9322(03)
792 00111-3.

793 Barbagallo, J., 2014: Aircraft wake turbulence. Advisory Circular 90-23G, Federal Aviation Ad-
794 ministration.

795 Barbaresco, F., 2012: Radar/lidar sensors for wind & wake-vortex monitoring on air-
796 port: First results of SESAR P12.2.2 XP0 trials campaign at Paris CDG airport.
797 <http://www.wakenet.eu/index.php?id=185>, Presentation slides for 4th Major Workshop of
798 WakeNet3-Europe.

799 Barbaresco, F., V. Brion, and N. Jeannin, 2016: Radar wake-vortices cross-section/doppler signa-
800 ture characterisation based on simulation and field tests trials. *IET Radar, Sonar & Navigation*,
801 **10 (1)**, 82–96, doi:10.1049/iet-rsn.2015.0132.

802 Barbaresco, F., P. Brovelli, P. Currier, O. Garouste, M. Klein, P. Juge, Y. Ricci, and J. Schneider,
803 2012: Radar sensors for wind & wake-vortex monitoring on airport: First results of SESAR

804 P12.2.2.2 XP0 trials campaign at Paris CDG airport. *Proc. 7th European Conference on Radar*
 805 *in Meteorology and Hydrology (ERAD 2012)*.

806 Barbaresco, F., J. Wasselin, A. Jeantet, and U. Meier, 2008: Wake vortex profiling by doppler
 807 X-band radar: Orly trials at initial take-off & ILS interception critical areas. *Proc. IEEE Radar*
 808 *Conference*, IEEE, doi:10.1109/RADAR.2008.4721113.

809 Barbaresco, F., and Coauthors, 2014: Radar 3D monitoring of wake-vortex hazards, circulation
 810 and EDR retrieval/calibration. *Proc. 2014 International Radar Conference*, IEEE, 1–7, doi:
 811 dx.doi.org/10.1109/RADAR.2014.7060419.

812 Batchelor, G., 1967: *An Introduction to Fluid Dynamics*. Cambridge University Press.

813 Beckmann, P., 1962: Statistical distribution of the amplitude and phase of a multiply scattered
 814 field. *J. of Res. of the Nat. Bureau of Standards—D. Radio Propagation*, **66D (3)**, 231–240,
 815 doi:10.6028/jres.066D.026.

816 Broderick, A., and Coauthors, 2008: Wake turbulence—An obstacle to increased air traffic capac-
 817 ity. Report, National Research Council of the National Academies.

818 Crouch, J., G. Miller, and P. Spalart, 2001a: Active-control system for breakup of airplane trailing
 819 vortices. *AIAA J.*, **39 (12)**, 2374–2381.

820 Crouch, J., G. Miller, and P. Spalart, 2001b: Development of an active system to break up trailing
 821 vortices. *Aero Magazine*, **(14)**, 24–31.

822 Doviak, R., and D. Zrnić, 1984: *Doppler Radar and Weather Observations*. Academic Press,
 823 Orlando, Florida.

824 Doyle, T., and F. McGee, 1998: Air traffic and operational data on selected U.S. airports with
 825 parallel runways. Tech. Rep. CR-1998-207675, NASA.

826 French, M. M., H. B. Bluestein, I. PopStefanija, C. A. Baldi, and R. T. Bluth, 2014: Mobile,
827 phased-array, doppler radar observations of tornadoes at X band. *Mon. Wea. Rev.*, **142**, 1010–
828 1036, doi:10.1175/MWR-D-13-00101.1.

829 Fritz, B., and W. Hoffmann, 2015: Update to the USDA-ARS fixed-wing spray nozzle mod-
830 els. *Trans. Am. Soc. Agri. & Bio. Engineers (ASABE)*, **58 (2)**, 281–295, doi:10.13031/trans.58.
831 10896.

832 Gilson, W., 1992: Aircraft wake RCS measurement. Project Report AAW-11, MIT Lincoln Labo-
833 ratory, Lexington, Mass.

834 Görsdorf, U., V. Lehmann, M. Bauer-Pfundstein, G. Peters, D. Vavriv, V. Vinogradov, and
835 V. Volkov, 2015: A 35-GHz polarimetric doppler radar for long-term observations of cloud
836 parameters—Description of system and data processing. *J. Atmos. & Oceanic. Tech.*, **32**, 675–
837 690, doi:10.1175/JTECH-D-14-00066.1.

838 Haller, G., and T. Sapsis, 2008: Where do inertial particles go in fluid flows. *Physica D*, **237**,
839 573–583, doi:10.1016/j.physd.2007.09.027.

840 Hamazu, K., H. Hashiguchi, T. Wakayama, T. Matsuda, R. Doviak, and S. Fukao, 2003: A 35-
841 GHz scanning doppler radar for fog observations. *J. Atmos. Oceanic Tech.*, **20**, 972–986, doi:
842 10.1175/1520-0426(2003)20<972:AGSDRF>2.0.CO;2.

843 Harris, F., 1978: On the use of windows for harmonic analysis with discrete fourier transforms.
844 *Proc. IEEE*, **66**, 55–83.

845 Ishimaru, A., 1978: *Wave Propagation and Scattering in Random Media*, Vol. 1. Academic Press,
846 New York.

847 Keränen, R., and V. Chandrasekhar, 2014: Detection and estimation of radar reflectivity from weak
848 echo of precipitation in dual-polarized weather radars. *J. Atmos. Oceanic Tech.*, **31**, 1677–1693,
849 doi:10.1175/JTECH-D-13-00155.1.

850 Kollias, P., N. Bharadwaj, K. Widener, I. Jo, and K. Johnson, 2014: Scanning ARM cloud radars.
851 Part I: Operational sampling strategies. *J. Atmos. Oceanic Tech.*, **31**, 569–582, doi:10.1175/
852 JTECH-D-13-00044.1.

853 Kollias, P., E. Clothiaux, M. Miller, B. Albrecht, G. Stephens, and T. Ackerman, 2007: Millimeter-
854 wavelength radars. New frontier in atmospheric cloud and precipitation research. *Bull. Am. Met.*
855 *Soc.*, **88** (10), 1608–1624, doi:10.1175/BAMS-88-10-1608.

856 Lefebvre, A., 1989: *Atomization and Sprays*. Hemisphere, New-York.

857 Li, J., T. Wang, L. Qu, H. Wang, and X. Wang, 2016: Circulation retrieval of wake vortex in fog
858 with an upward-looking monostatic radar. *IEEE Trans. Aerospace & Electronic Systems*, **52** (1),
859 169–180, doi:10.1109/TAES.2015.140901.

860 Li, J., X. Wang, and T. Wang, 2011: Modeling the dielectric constant distribution of wake vor-
861 tices. *IEEE Trans. Aerospace & Electronic Systems*, **47** (2), 820–830, doi:10.1109/TAES.2011.
862 5751228.

863 Liebe, H., G. Hufford, and T. Manabe, 1991: A model for the complex permittivity of water at
864 frequencies below 1 THz. *Int. J. Infrared & Millimeter Waves*, **12** (7), 659–675, doi:10.1007/
865 BF01008897.

866 Liu, Z., N. Jeannin, F. Vincent, and X. Wang, 2013: Modeling the radar signature of rain-
867 drops in aircraft wake vortices. *J. Atmos. Oceanic Technol.*, **30** (3), 470–484, doi:10.1175/
868 JTECH-D-11-00220.1.

869 Lorenzetto, G., and A. Lefebvre, 1977: Measurements of drop size on a plain-jet airblast atomizer.
 870 *AIAA J.*, **15** (7), 1006–1010, doi:10.2514/3.60742.

871 Pruppacher, H., and J. Klett, 1997: *Microphysics of clouds and precipitation*. Kluwer, Dordrecht.

872 Radhakrishnan, K., and A. Hindmarsh, 1993: Description and use of LSODE, the Livermore
 873 solver of ordinary differential equations. Reference Publication 1327, NASA.

874 Rayleigh, J., 1945: *Theory of Sound*, Vol. 1. Dover, New York.

875 Sapsis, T., and G. Haller, 2010: Clustering criterion for inertial particles in two-dimensional time-
 876 periodic and three-dimensional steady flows. *Chaos*, **20**, 017 515:1–11, doi:10.1063/1.3272711.

877 Seliga, T., and J. Mead, 2009: Meter-scale observations of aircraft wake vortices in pre-
 878 cipitation using a high resolution solid-state W-band radar. *34th Conf. on Radar Mete-*
 879 *orology*, American Meteorological Society, P10.25, extended abstract available online as
 880 <https://ams.confex.com/ams/pdfpapers/155796.pdf>.

881 Shariff, K., and A. Wray, 2002: Analysis of the radar reflectivity of aircraft vortex wakes. *J. Fluid*
 882 *Mech.*, **463**, 121–161, doi:10.1017/S0022112002008674.

883 Spalart, P., 1996: On the motion of laminar wing wakes in a stratified fluid. *J. Fluid Mech.*, 139–
 884 160, doi:10.1017/S002211209600849X.

885 Spalart, P., 1998: Airplane trailing vortices. *Ann. Rev. Fluid Mech.*, **30**, 107–138, doi:10.1146/
 886 annurev.fluid.30.1.107.

887 Vanhoenacker-Janvier, D., D. Kahina, and F. Babaresco, 2012: Model for the calculation of the
 888 radar cross section of wake vortices of take-off and landing airplanes. *Proc. 9th European Radar*
 889 *Conference (EuRAD)*, IEEE, 349–352.

890 Varga, C., J. Lasheras, and E. Hopfinger, 2003: Initial breakup of a small-diameter liquid jet by a
891 high-speed gas stream. *J. Fluid Mech.*, **497**, 405–434.

892 Widener, K., N. Bharadwaj, and K. Johnson, 2012: Scanning ARM cloud radar (X/Ka/W-SACR).
893 Tech. Rep. DOE/SC-ARM/TR-113, U.S. Dept. of Energy, Office of Science, Office of Biologi-
894 cal and Environmental Research.

895 Yuter, S., 2003: Precipitation radar. *Encyclopedia of Atmospheric Sciences*, J. Holton, J. Pyle, and
896 J. Curry, Eds., Academic Press, Amsterdam, 1833–1851.

897	LIST OF TABLES	
898	Table 1. IFR separation standards (in nautical miles) for arrivals on the same runway	
899	(Barbagallo 2014).	46
900	Table 2. Aerial nozzle parameters for the operating conditions specified. Notes: 1: ‘Str’	
901	denotes a straight-stream. 2: Values obtained from B. Fritz’s Excel program.	
902	3: See text for how flow-rates were obtained.	47
903	Table 3. Parameters of a typical heavy aircraft.	48
904	Table 4. Radar parameters. EEC: Enterprise Electronics Corp; PRF: Pulse repetition	
905	frequency. Note 1: nnn is the power in kW (250, 350, 500, or 1000). Note	
906	2: The only value provided to us was for MIRA-35. The value for the other	
907	radars was assumed to be the same. Note 3: The value for a perfectly matched	
908	filter has been assumed for all radars. Note 4: For a rainfall rate of 12.5 mm/hr	
909	(medium to heavy rain). Note 5: MIRA-35 has full sensitivity beyond a range	
910	of 360 m (Matthias Bauer-Pfundstein, Private communication).	49
911	Table 5. Yearly-averaged temperature and humidity when IFR conditions prevail at the	
912	five busiest US airports.	50
913	Table 6. A comparison of SNR1 reflectivity obtained from a single range cell by using	
914	the four different nozzles listed in Table 2. A comparison with the simple <i>a</i>	
915	<i>priori</i> measure, $\xi_{\text{nozzle}}^{<}$, of nozzle performance is also shown. The cell center	
916	is at $(x, y, z) = (6 \text{ nm}, -50 \text{ m}, -230 \text{ m})$. The signed values (\pm) indicate values	
917	<i>relative to nozzle 1</i> . MIRA-35, $\tau = 0.2 \mu\text{s}$, $\theta_b = 0.52^\circ$	51

Leader	Follower				
	Super	Heavy	B757	Large	Small
Super	3	6	7	7	8
Heavy	3	4	5	5	6
B757	3	4	4	4	5
Large	3	3	3	3	4
Small	3	3	3	3	3

TABLE 1. IFR separation standards (in nautical miles) for arrivals on the same runway (Barbagallo 2014).

	Nozzle 1	Nozzle 2	Nozzle 3	Nozzle 4
Model	CP-09	CP-09	CP11TT	Davidon-Triset
Pressure (psi)	90	90	90	90
Airspeed (mph)	175	175	175	175
Deflection-plane/body angle	0°	0°	0°	0°
Fan angle	Str. ¹	Str.	Str.	Str.
Orifice Code			20	
Orifice diameter (in)	0.125	0.172	0.105	0.125
$a_{0.5}$ (μm) ^{Note 2}	178.5	146.5	183	239.5
$a_{0.9}$ (μm) ^{Note 2}	315	303	359	463
a_0 of log-normal	99.02	55.83	79.85	108.3
σ of log-normal	0.443	0.567	0.526	0.514
Flow-rate (gpm) ^{Note 3}	3.70	6.49	3.00	3.06
U_{exit} (m s^{-1})	29.5	27.3	33.9	24.4
No. of nozzles per side	1	1	1	1
Gallons per nm (two sides)	2.96	5.19	2.4	2.45

918 TABLE 2. Aerial nozzle parameters for the operating conditions specified. Notes: 1: ‘Str’ denotes a straight-
919 stream. 2: Values obtained from B. Fritz’s Excel program. 3: See text for how flow-rates were obtained.

Parameter	Value
Weight, W	500,000 lb
Wing span, b	60 m
Vortex spacing, b_0	47.9 m
Vortex circulation, Γ	$526 \text{ m}^2 \text{ s}^{-1}$
Approach speed, U_{app}	150 knots

TABLE 3. Parameters of a typical heavy aircraft.

Manufacturer	EEC	EEC	EEC	Metek	ProSensing
Series	DWSR	DWSR	DWSR		
Model	8501S	nnn1C ^{Note 1}	2001X	MIRA-35	W-SACR
Frequency, f (GHz)	3	5.9	9.6	35.1	93.9
Peak power, P_t (kW)	850	250–1000	200	30	1.7
Reflector diameter (m)	4.2	4.2	2.4	1.2,2.0	0.9
$\frac{1}{2}$ -power beam width, θ_b	1.83°	0.95°	0.95°	0.52°,0.31°	0.30°
Antenna gain, G (dB)	39.5	45	45	50.4,53.5	54.5
Pulse width, τ (μ s)	0.4–2	0.2–3	0.2–2	0.1,0.2,0.4	0.05–2
Range resolution, $c\tau/2$ (m)	60–300	30–450	30–300	15,30,60	7.5–300
PRF (kHz)	0.2–2.4	0.2–2.4	0.2–2.4	2.5,5,10	≤ 20
$U_{\max} = c \text{ PRF}/4f$ (m s ⁻¹)	5–60	2.5–31	1.6–19	5.3,11,21	≤ 16
Receiver noise figure (dB)	2.0	2.0	2.0	6.2	6.0
2-way waveguide loss ^{Note 2} (dB)	0.8	0.8	0.8	0.8	0.8
Finite bandwidth loss ^{Note 3} (dB)	1.8	1.8	1.8	1.8	1.8
Rain attenuation ^{Note 4} (dB/km)	0.005	0.03	0.12	2	7
Minimum range (m)				150 ^{Note 5}	

TABLE 4. Radar parameters. EEC: Enterprise Electronics Corp; PRF: Pulse repetition frequency. Note 1: nnn
 is the power in kW (250, 350, 500, or 1000). Note 2: The only value provided to us was for MIRA-35. The
 value for the other radars was assumed to be the same. Note 3: The value for a perfectly matched filter has been
 assumed for all radars. Note 4: For a rainfall rate of 12.5 mm/hr (medium to heavy rain). Note 5: MIRA-35 has
 full sensitivity beyond a range of 360 m (Matthias Bauer-Pfundstein, Private communication).

Airport	T (C)	RH	% IFR Reports
ATL	12.5	95.5%	5.3%
LAX	15.2	92.7%	3.5%
DFW	9.7	94.5%	1.4%
ORD	5.3	94.2%	3.7%
JFK	12.1	93.9%	4.8%

TABLE 5. Yearly-averaged temperature and humidity when IFR conditions prevail at the five busiest US airports.

Nozzle no.	gpm	SNR1 (dB)	$\dot{\zeta}_{\text{nozzle}}^< \text{ (dB m}^6 \text{ s}^{-1}\text{)}$	$\zeta_x \text{ (dB m}^5\text{)}$
near vortex at $x = 6 \text{ nm}$				
1	3.70	19.15	-157.4	-178.8
2	6.49	+1.03	+1.0	+0.6
3	3.00	-1.04	-1.2	-1.4
4	3.06	-0.5	-0.3	-1.0

TABLE 6. A comparison of SNR1 reflectivity obtained from a single range cell by using the four different nozzles listed in Table 2. A comparison with the simple *a priori* measure, $\dot{\zeta}_{\text{nozzle}}^<$, of nozzle performance is also shown. The cell center is at $(x, y, z) = (6 \text{ nm}, -50 \text{ m}, -230 \text{ m})$. The signed values (\pm) indicate values *relative* to nozzle 1. MIRA-35, $\tau = 0.2 \mu\text{s}$, $\theta_b = 0.52^\circ$.

LIST OF FIGURES

Fig. 1.	(a) Probability density function (pdf) of the drop sizes produced by nozzle 1 with the conditions listed in Table 2. The result is based on parameters provided by B. Fritz's Excel program. (b) Distance required for a droplet of a given size to begin moving with an imposed air flow.	54
Fig. 2.	Back-scattering cross-section σ_b (normalized by the Rayleigh value) and phase-shift ϕ versus droplet radius a at the frequencies considered in this work.	55
Fig. 3.	Temperature and humidity (averaged by month) when IFR conditions prevail at the five busiest U.S. airports	56
Fig. 4.	Simulated SNR1 for five radars in a range-elevation scan of the $x = 6$ nm cross-section behind the aircraft. Panel (a) shows droplets colored by radius in μm . IFR ambient conditions: RH = 92.7%, $T = 15.2$ C. Nozzle 1.	57
Fig. 5.	Effect of pulse width and beam width on simulated SNR1. (a) W-SACR with a pulse width of $0.05 \mu\text{s}$; (b) Difference in SNR1 (dB) when MIRA-35 is used with a beam width of $\theta_b = 0.31^\circ$ compared to $\theta_b = 0.52^\circ$. $x = 6$ nm cross-section of the wake. IFR ambient conditions. Nozzle 1.	58
Fig. 6.	Insensitivity to the initial condition. For panels (a) and (b) droplets were placed randomly on each $1 \text{ m} \times 1 \text{ m}$ square. For (c) and (d) droplets were arranged on a regular grid on each $50 \text{ cm} \times 50 \text{ cm}$ square.	59
Fig. 7.	Gray line: Instantaneous power $P_r(t)$ received from the same range gate due to a sequence of transmitted pulses. The range cell is at $(x, y, z) = (6 \text{ nm}, -50 \text{ m}, -230 \text{ m})$. Green: received powers averaged over segments 512 pulses long. Red: the first term in (23). Panels (a)–(c) are for the same cases as in Figure 4d–f.	60
Fig. 8.	Convergence of pulse statistics when the number of computational droplets is increased by four. The same case as Figure 7d is used (MIRA-35 radar). Note: The solid and dashed lines are nearly coincident.	61
Fig. 9.	SNR1 for a non-IFR condition (RH = 60%, $T = 20$ C). A range elevation scan of the wake cross-section 6 nm behind the aircraft is shown. The white circles in panel (e) are points for which a spectral analysis is presented in Figure 10.	62
Fig. 10.	Detection at low SNR1 using spectral processing. Panels (a) and (b) are for the the resolution cell centered on $(x, y, z) = (6 \text{ nm}, -55 \text{ m}, -260 \text{ m})$ which is shown as the white circle to the left in Figure 9e. Panels (c) and (d) are for $(x, y, z) = (6 \text{ nm}, -15 \text{ m}, -255 \text{ m})$ which is shown as the white circle to the right in Figure 9e. The radar is MIRA-35 with $\tau = 0.2 \mu\text{s}$ and PRF = 10 kHz. Non-IFR condition (RH = 60%, $T = 20$ C).	63
Fig. 11.	Power-weighted radial velocity corresponding to Figure 4. Only points where SNR1 > 1 are colored. The actual radial velocity of the gas is shown in panel (a).	64
Fig. 12.	(a) ζ_x for a droplet trail on one side of the aircraft. “Near the vortex” curves (dashed) were obtained by considering only those droplets that obey $ y < 60 \text{ m}$ and $ z - z_{\text{vort}} < 35 \text{ m}$, z_{vort} being the height of the vortex center. IFR ambient humidity and temperature were assumed. (b) Droplet size distributions produced by the four nozzles. The solid lines show the exact	

969 log-normal distribution, while the symbols show the distribution for each sample of 27,000
 970 droplets injected into the wake. 65

971 **Fig. 13.** SNR1 at different azimuthal angles for the Mira-35 radar located at $x_{\text{rad}} = 4$ nm. The az-
 972 imuthal angle is measured clockwise relative to normal incidence. A vertical line at $y = 0$ in
 973 the scanning plane is located at the following axial locations behind the aircraft for the three
 974 plots: (a) $x = 2$ nm; (b) $x = 4$ nm; (c) $x = 6$ nm. IFR ambient conditions ($\text{RH} = 92.7\%$, $T =$
 975 15.2 C). Nozzle 1. 66

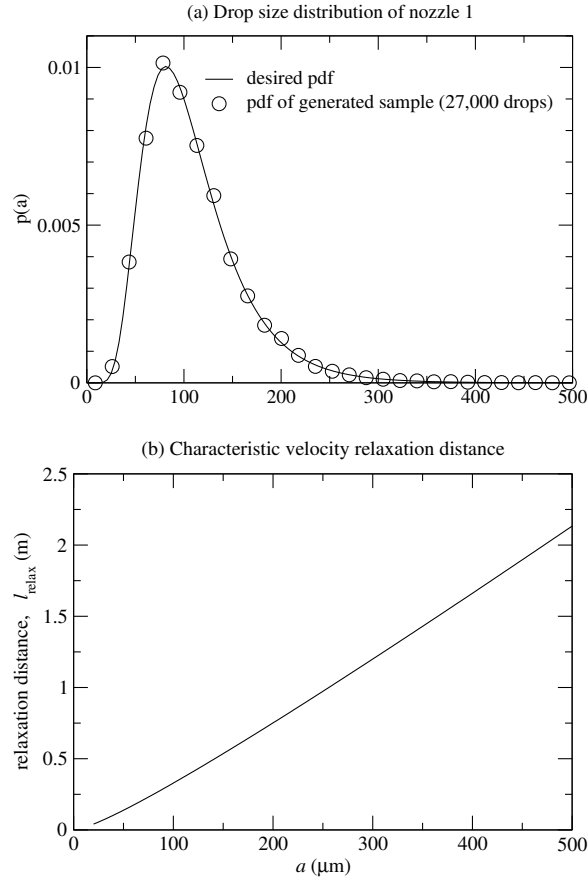
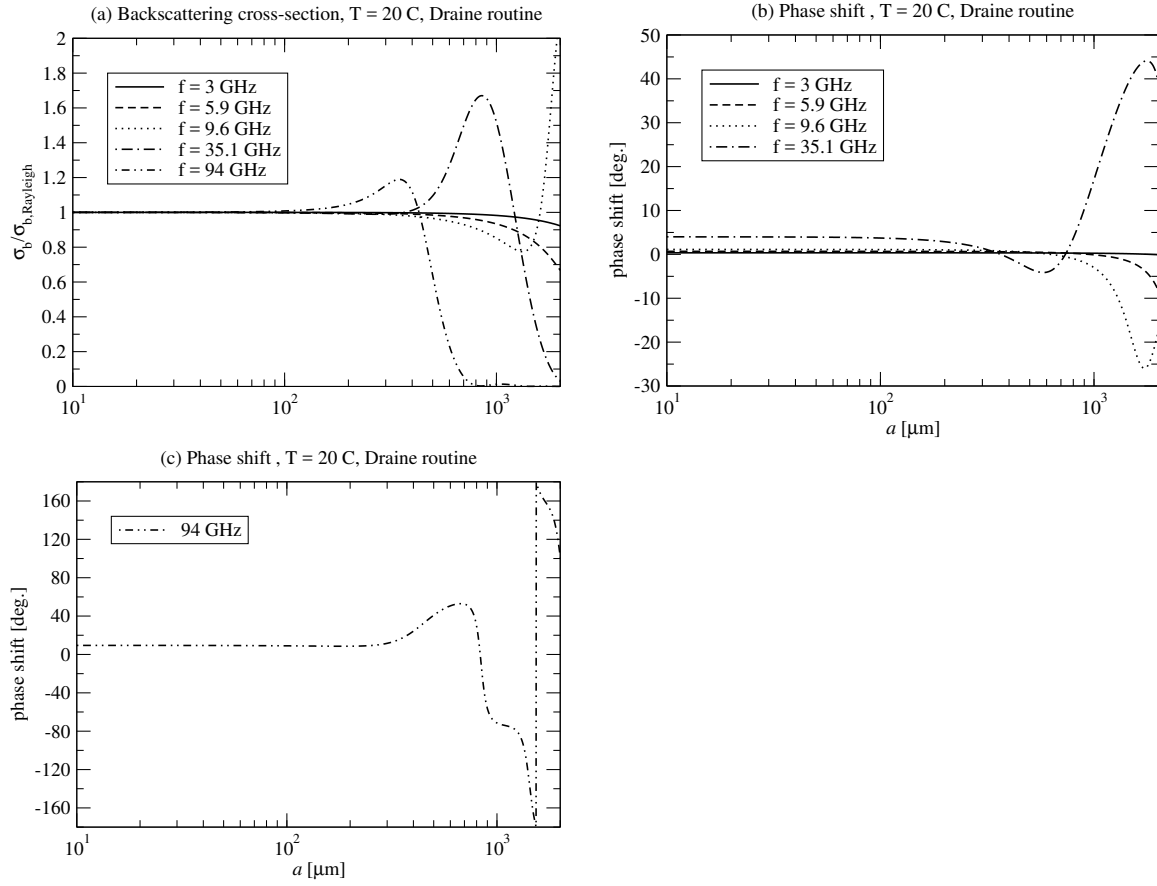


FIG. 1. (a) Probability density function (pdf) of the drop sizes produced by nozzle 1 with the conditions listed in Table 2. The result is based on parameters provided by B. Fritz's Excel program. (b) Distance required for a droplet of a given size to begin moving with an imposed air flow.



979 FIG. 2. Back-scattering cross-section σ_b (normalized by the Rayleigh value) and phase-shift ϕ versus droplet
 980 radius a at the frequencies considered in this work.

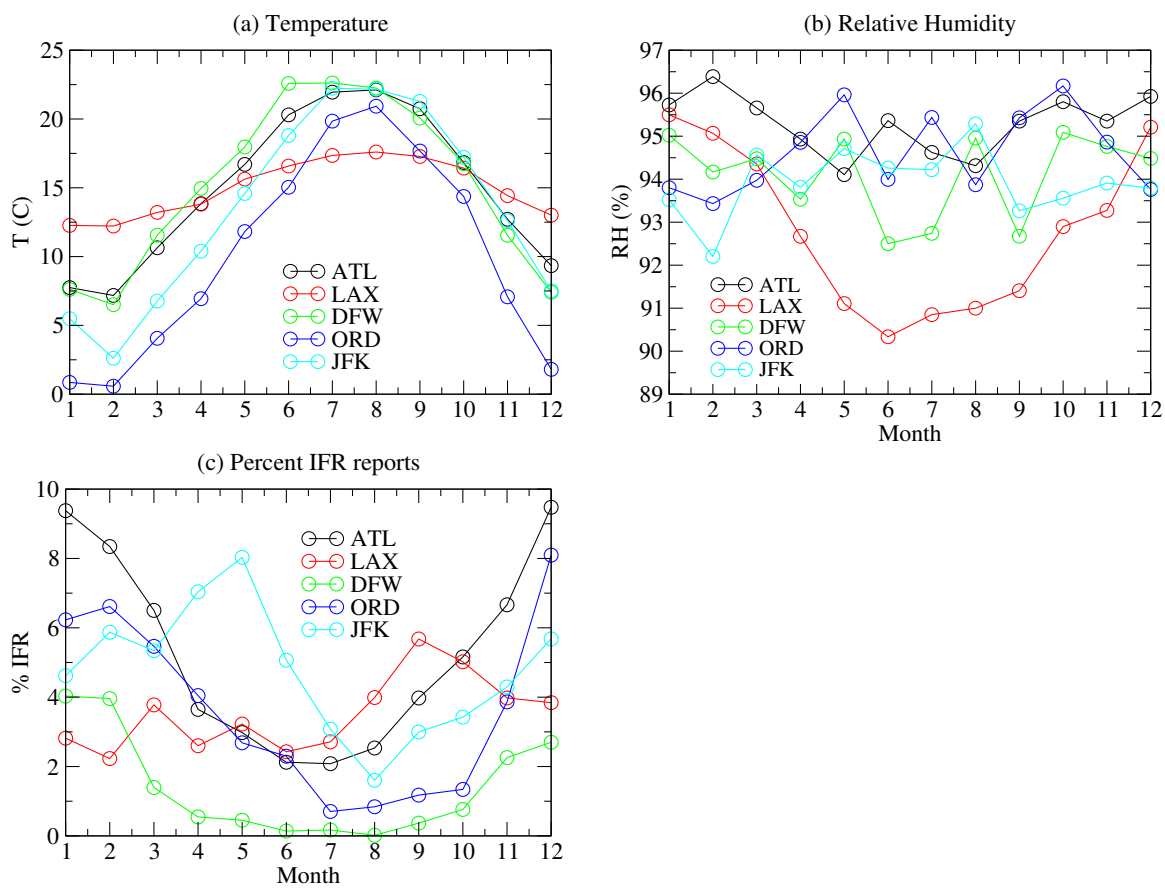


FIG. 3. Temperature and humidity (averaged by month) when IFR conditions prevail at the five busiest U.S. airports

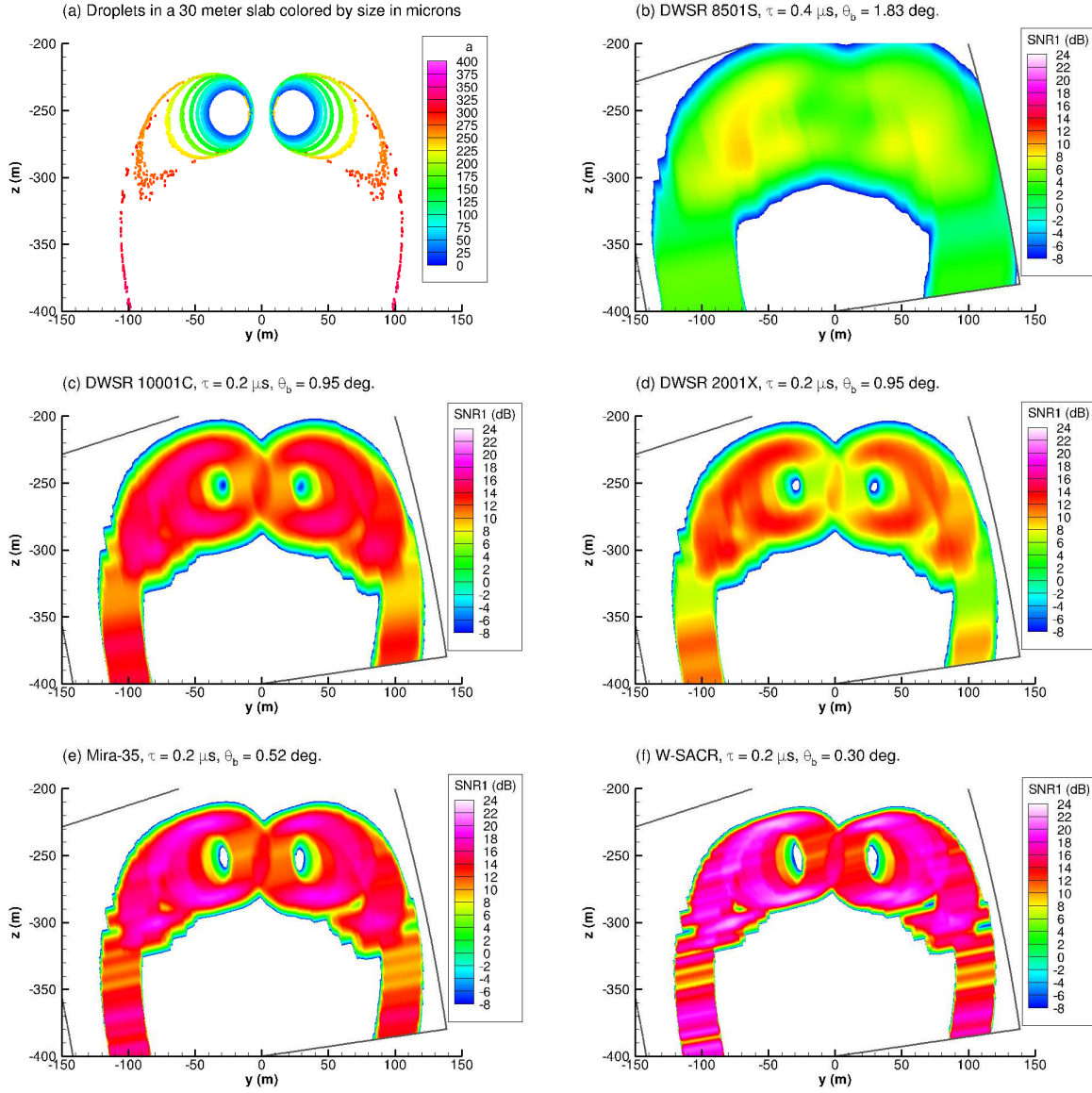
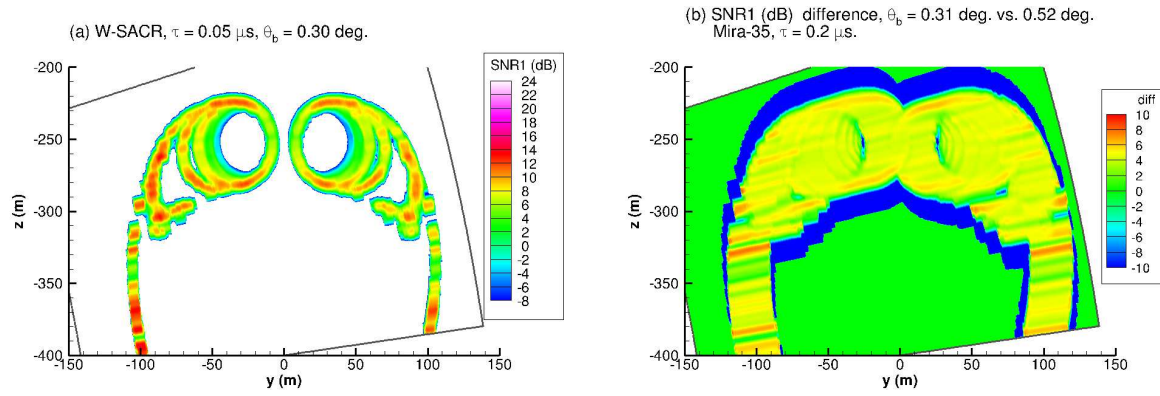


FIG. 4. Simulated SNR1 for five radars in a range-elevation scan of the $x = 6 \text{ nm}$ cross-section behind the aircraft. Panel (a) shows droplets colored by radius in μm . IFR ambient conditions: $\text{RH} = 92.7\%$, $T = 15.2 \text{ C}$. Nozzle 1.



986 FIG. 5. Effect of pulse width and beam width on simulated SNR1. (a) W-SACR with a pulse width of $0.05 \mu\text{s}$;
 987 (b) Difference in SNR1 (dB) when MIRA-35 is used with a beam width of $\theta_b = 0.31^\circ$ compared to $\theta_b = 0.52^\circ$.
 988 $x = 6 \text{ nm}$ cross-section of the wake. IFR ambient conditions. Nozzle 1.

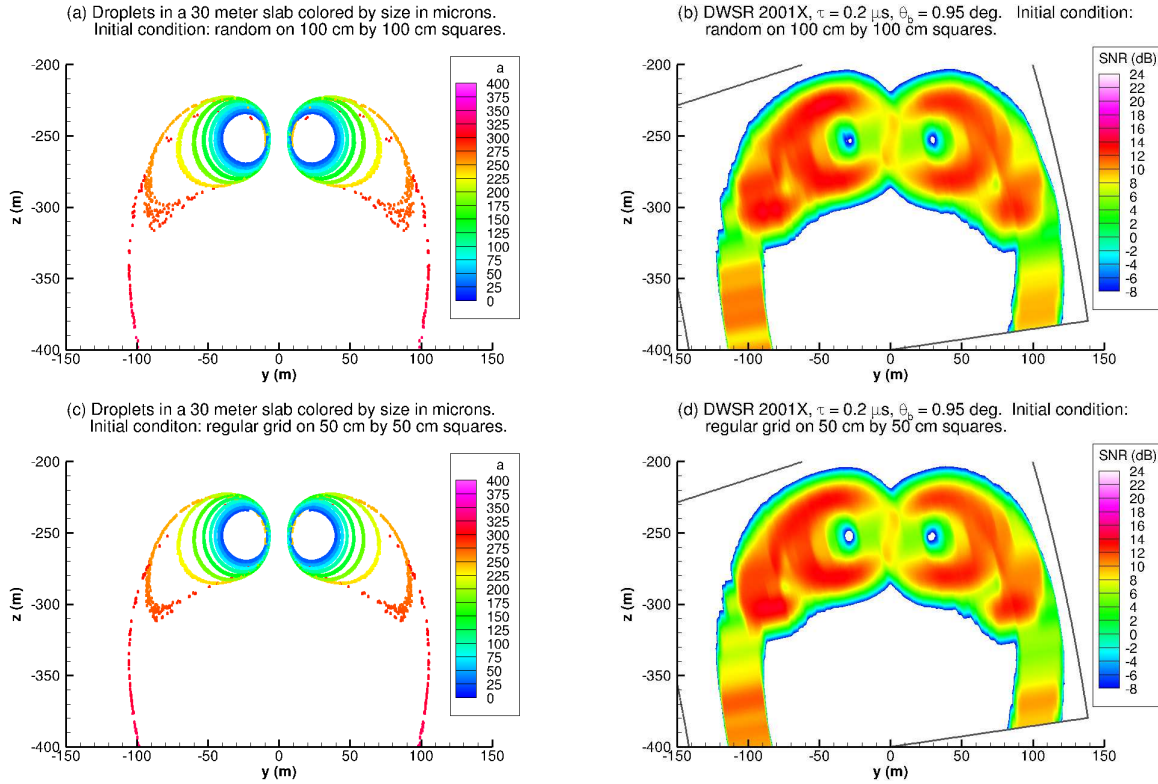


FIG. 6. Insensitivity to the initial condition. For panels (a) and (b) droplets were placed randomly on each $1 \text{ m} \times 1 \text{ m}$ square. For (c) and (d) droplets were arranged on a regular grid on each $50 \text{ cm} \times 50 \text{ cm}$ square.

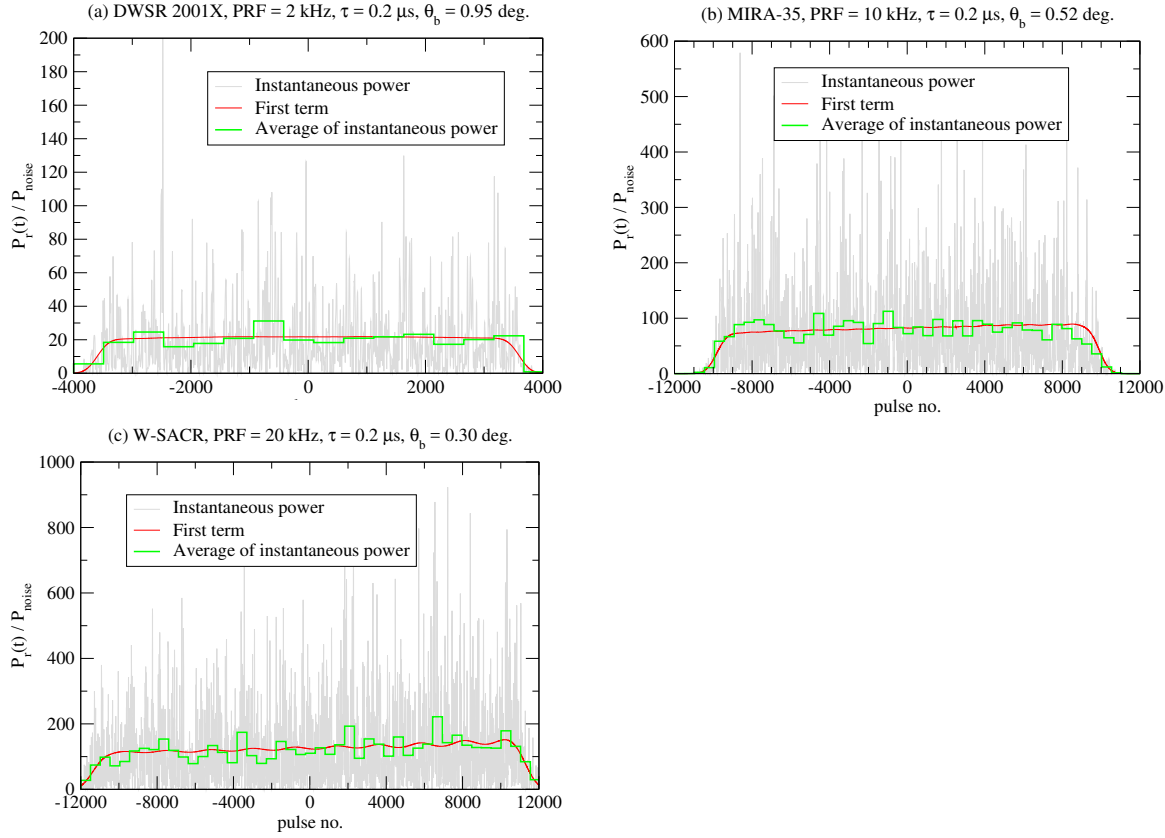
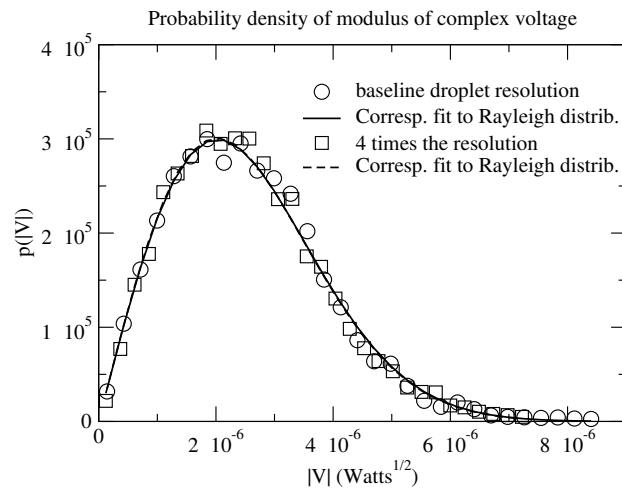


FIG. 7. Gray line: Instantaneous power $P_r(t)$ received from the same range gate due to a sequence of transmitted pulses. The range cell is at $(x, y, z) = (6 \text{ nm}, -50 \text{ m}, -230 \text{ m})$. Green: received powers averaged over segments 512 pulses long. Red: the first term in (23). Panels (a)–(c) are for the same cases as in Figure 4d–f.



994 FIG. 8. Convergence of pulse statistics when the number of computational droplets is increased by four. The
 995 same case as Figure 7d is used (MIRA-35 radar). Note: The solid and dashed lines are nearly coincident.

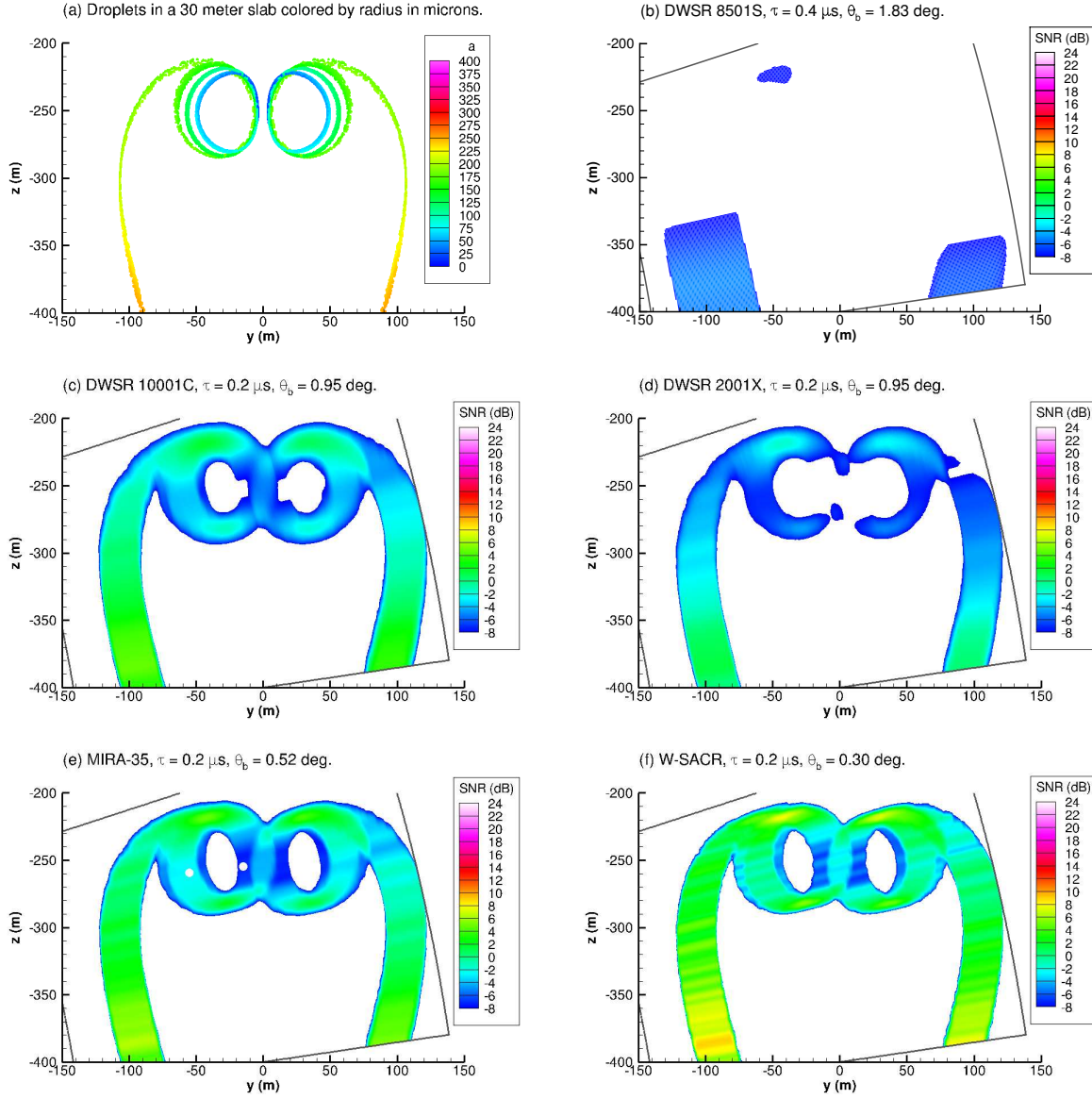


FIG. 9. SNR1 for a non-IFR condition ($\text{RH} = 60\%$, $T = 20 \text{ C}$). A range elevation scan of the wake cross-section 6 nm behind the aircraft is shown. The white circles in panel (e) are points for which a spectral analysis is presented in Figure 10.

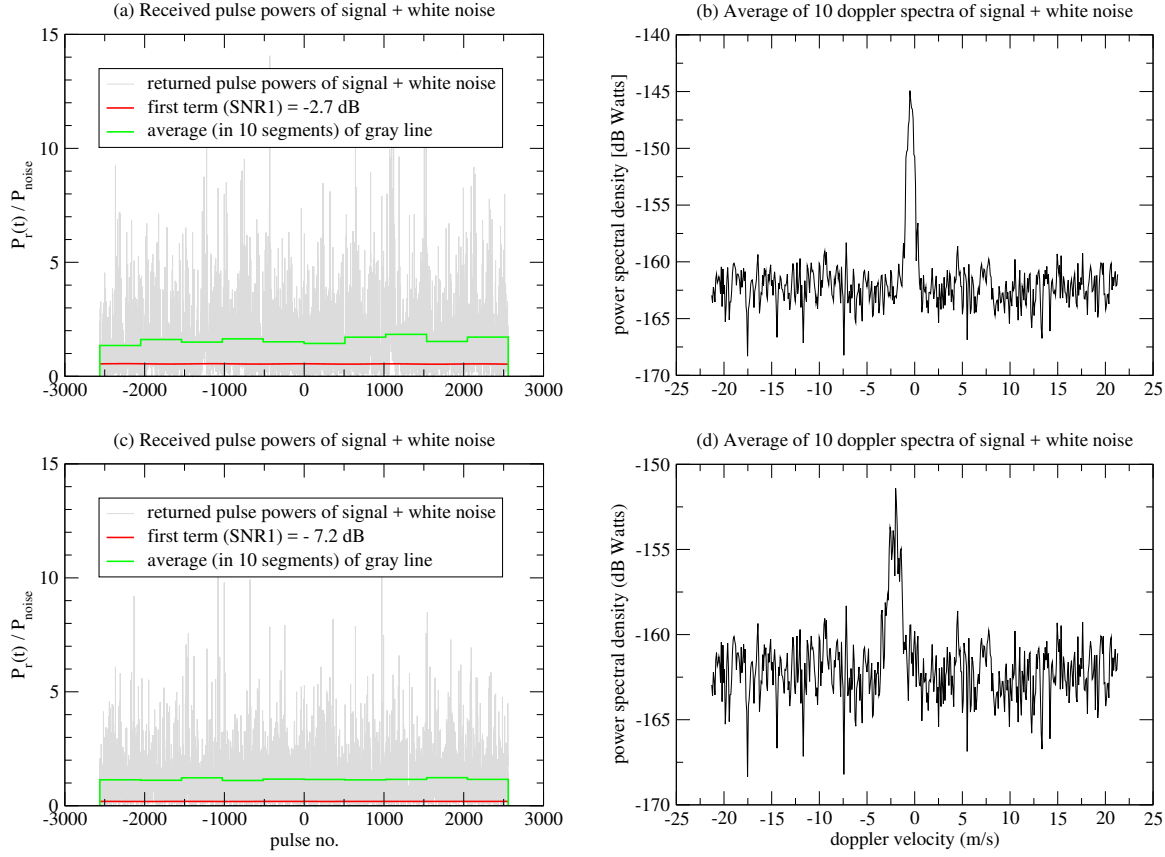


FIG. 10. Detection at low SNR1 using spectral processing. Panels (a) and (b) are for the the resolution cell centered on $(x, y, z) = (6 \text{ nm}, -55 \text{ m}, -260 \text{ m})$ which is shown as the white circle to the left in Figure 9e. Panels (c) and (d) are for $(x, y, z) = (6 \text{ nm}, -15 \text{ m}, -255 \text{ m})$ which is shown as the white circle to the right in Figure 9e. The radar is MIRA-35 with $\tau = 0.2 \mu\text{s}$ and PRF = 10 kHz. Non-IFR condition (RH = 60%, $T = 20 \text{ C}$).

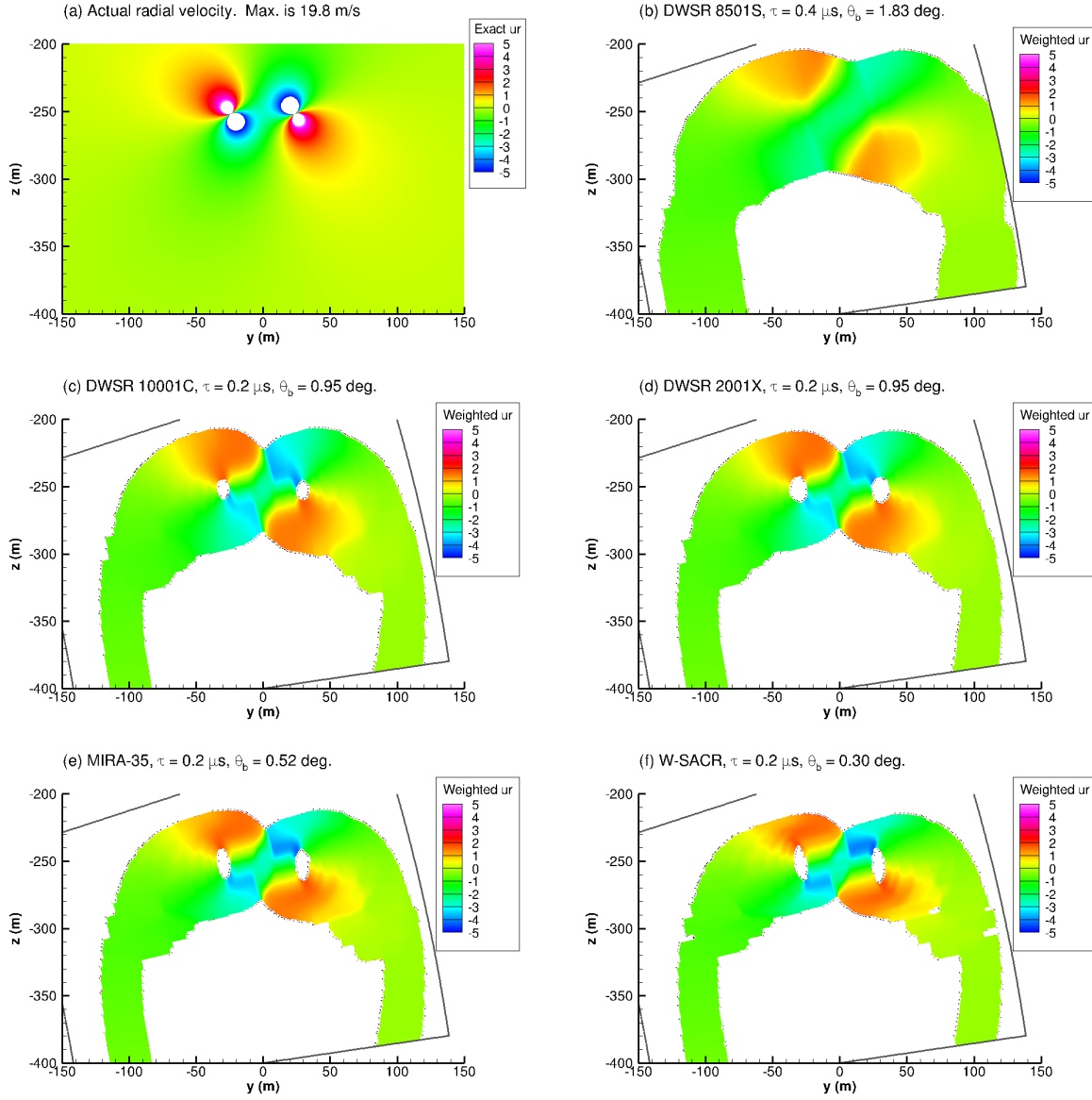


FIG. 11. Power-weighted radial velocity corresponding to Figure 4. Only points where $\text{SNR1} > 1$ are colored.

The actual radial velocity of the gas is shown in panel (a).

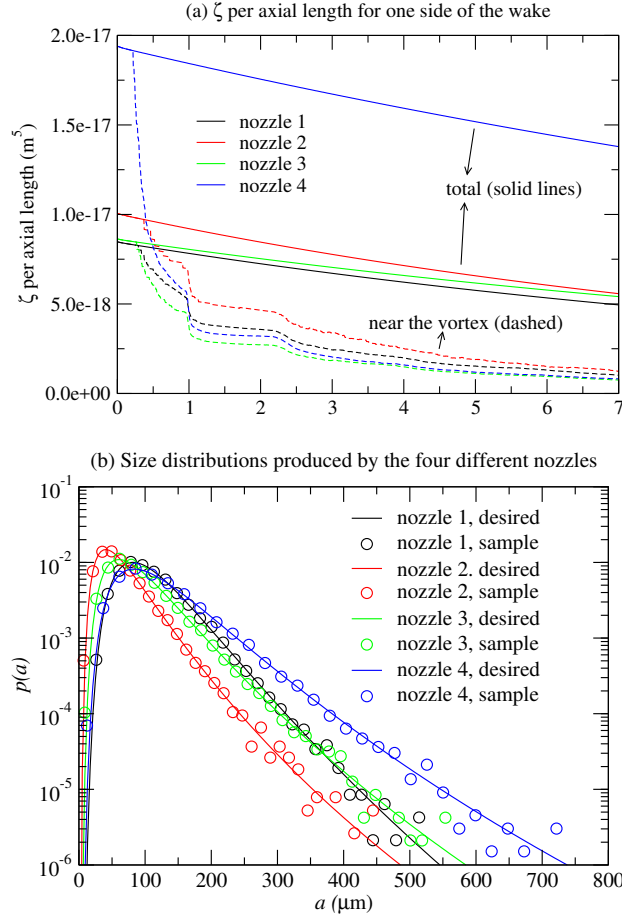


FIG. 12. (a) ζ_x for a droplet trail on one side of the aircraft. “Near the vortex” curves (dashed) were obtained by considering only those droplets that obey $|y| < 60$ m and $|z - z_{\text{vort}}| < 35$ m, z_{vort} being the height of the vortex center. IFR ambient humidity and temperature were assumed. (b) Droplet size distributions produced by the four nozzles. The solid lines show the exact log-normal distribution, while the symbols show the distribution for each sample of 27,000 droplets injected into the wake.

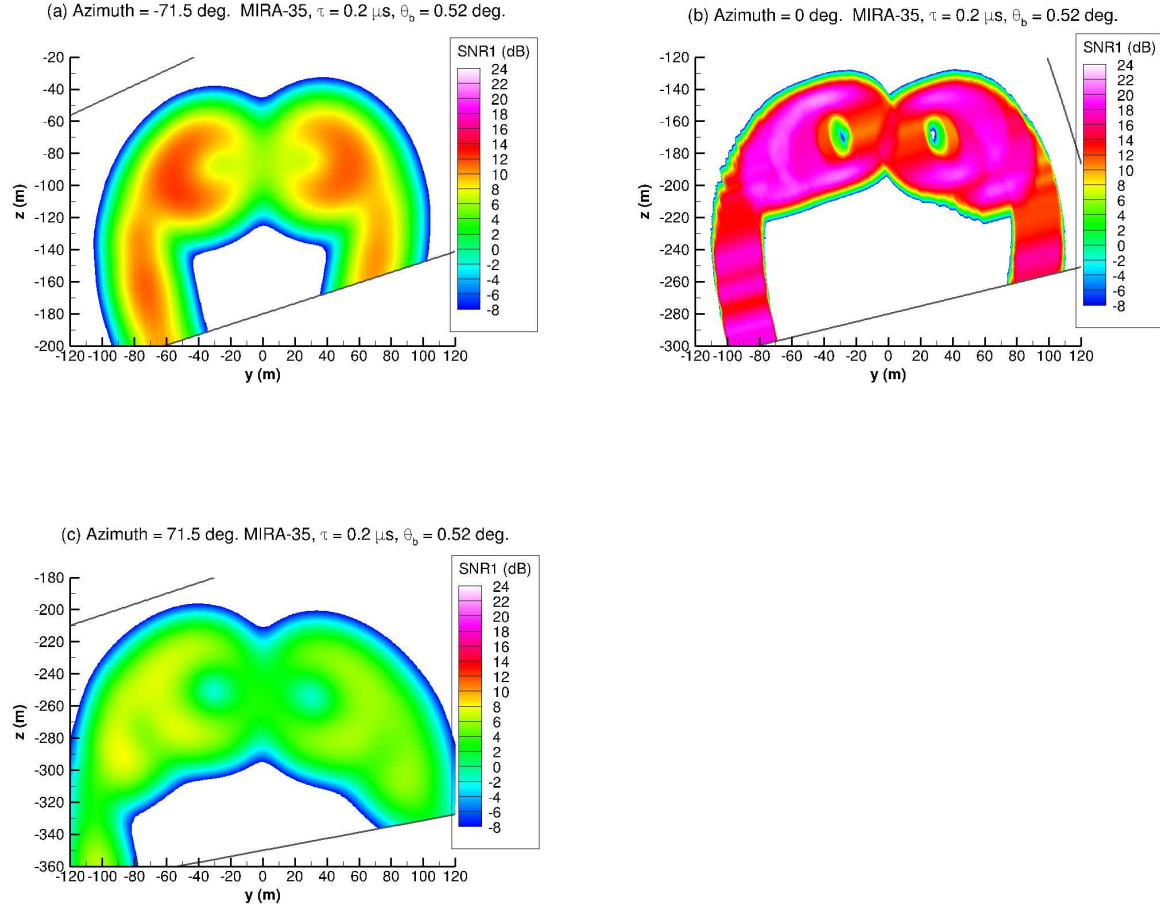


FIG. 13. SNR1 at different azimuthal angles for the Mira-35 radar located at $x_{\text{rad}} = 4 \text{ nm}$. The azimuthal angle is measured clockwise relative to normal incidence. A vertical line at $y = 0$ in the scanning plane is located at the following axial locations behind the aircraft for the three plots: (a) $x = 2 \text{ nm}$; (b) $x = 4 \text{ nm}$; (c) $x = 6 \text{ nm}$. IFR ambient conditions (RH = 92.7%, T = 15.2 C). Nozzle 1.